Dissociative Adsorption of CO2 on Copper: The Role of Steps

Hagman, Benjamin

2021

Document Version:
Publisher's PDF, also known as Version of record

Dissociative Adsorption of CO_2 on Copper: The Role of Steps

BENJAMIN HAGMAN
DEPARTMENT OF PHYSICS | FACULTY OF SCIENCE | LUND UNIVERSITY

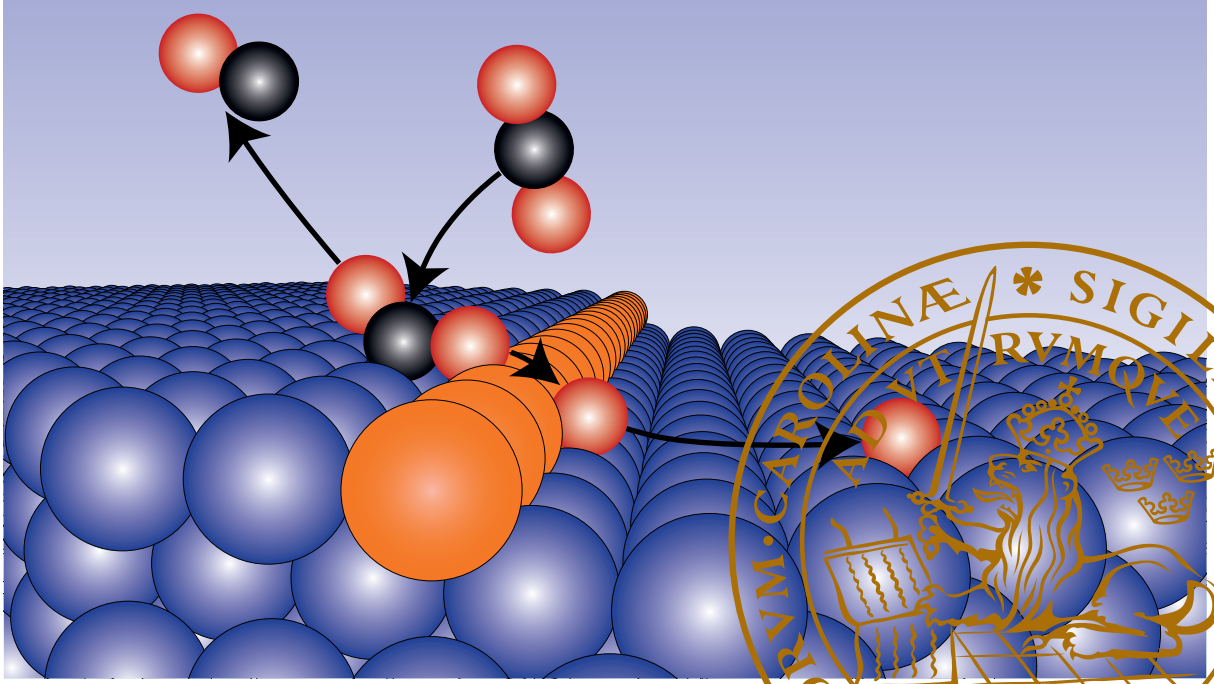

Printed by Media-Tryck, Lund 2021 NORDIC SWAN ECOLABEL 3041 0903

Faculty of Science
Department of Physics
Division of Synchrotron Radiation Research

ISBN 978-91-7895-962-4

Dissociative Adsorption of CO_2 on Copper: The Role of Steps

by Benjamin Hagman

LUND
UNIVERSITY

Doctoral thesis
Thesis advisors: Dr. Johan Gustafson, Prof. Edvin Lundgren
Faculty opponent: Prof. Bongjin Simon Mun

To be presented, with the permission of the Faculty of Science, Lund University, for public criticism in the lecture hall Rydbergsalen at the Department of Physics on Friday, the 24th of September 2021 at 09:15 pm.

Funding information: The thesis work was financially supported by Knut and Alice Wallenberg Foundation (19651218-4018, Atomistic Design of Catalysts).

Faculty of Science, Department of Physics, Division of Synchrotron Radiation Research

ISBN: 978-91-7895-962-4 (print)
ISBN: 978-91-7895-962-4 (pdf)

Printed in Sweden by Media-Tryck, Lund University, Lund 2021

Till Soraya

Contents

Preface

List of publications

This thesis is based on the following publications in which I have contributed to the experiments, the analysis of the experimental data, and the writing of the experimental parts in the papers.

I **Initial Oxidation of Cu(100) studied by X-ray photo-electron spectroscopy and density functional theory calculations**
A. Posada-Borbón, B. Hagman, A. Schaefer, C. Zhang, M. Shipilin, A. Hellman, J. Gustafson, and H. Grönbeck
Surf. Sci. **675** (2018), 64–69

My Contribution: I participated in the planning and execution of the experiments. I did all data analysis of the experimental data. I wrote about the experimental results in the paper.

II **Steps control the dissociation of CO_2 on Cu(100)**

B. Hagman, A. Posada-Borbón, A. Schaefer, M. Shipilin, C. Zhang, L. R. Merte, A. Hellman, E. Lundgren, H. Grönbeck, and J. Gustafson
J. Am. Chem. Soc. **140** (2018), 12974-12979

My Contribution: I participated in the planning and execution of the experiments. I did all data analysis of the experimental data. I wrote about the experimental results in the paper.

III **Oxygen induced faceting of Cu(911)**

B. Hagman. H. Edström, K. von Allmen, A. Schaefer, and J. Gustafson
Manuscript submitted to Surface Science.

My Contribution: I was responsible for the planning and execution of the experiments. I did all data analysis of the experimental data. I was the main responsible for writing the paper.

IV **Oxide growth on Cu(911)**

B. Hagman. H. Edström, K. von Allmen, A. Schaefer, and J. Gustafson
Manuscript in progress

My Contribution: I was responsible for the planning and execution of the experiments. I did all data analysis of the experimental data. I was the main responsible for writing the paper.

v **CO_2 dissociation on Cu(911)**

B. Hagman. A. Posada-Borbon, H. Edström, K. von Allmen, A. Schaefer, H. Grönbeck, and J. Gustafson
Manuscript in progress

My Contribution: I was responsible for the planning and execution of the experiments. I did all data analysis of the experimental data. I was the main responsible for writing the paper.

Papers not included in this thesis, to which I have contributed:

Thermal reduction of ceria nanostructures on rhodium(111) and re-oxidation by CO_2
A. Schaefer, B. Hagman, J. Höcker, U. Hejral, J. I. Flege, and J. Gustafson
Phys. Chem. Chem. Phys. **20** (2018), 19447

Catalytic Oxidation of Carbon Monoxide on a Curved Pd Crystal: Spatial Variation of Active and Poisoning Phases in Stationay Conditions
F. Schiller, M. Ilyn, V. Pérez-Dieste, C. Escudero, C. Huck-Iriart, N. R. del Arbol, B. Hagman, L. R. Merte, F. Bertram, M. Shipilin, S. Blomberg, J. Gustafson, E. Lundgren, and J. E. Ortega
J. Am. Chem. Soc. **140** (2018), 16245-16252

The Role of Oxides in Catalytic CO Oxidation over Rhodium and Palladium
J. Gustafson, O. Balmes, C. Zhang, M. Shipilin, A. Schaefer, B. Hagman, L. R. Merte, N. M. Martin P.-A. Carlsson, M. Jankowski, E. J. Crumlin, and E. Lundgren
ACS Catal. **8** (2018), 4438-4445

HIPPIE: a new platform for ambient-pressure X-ray photoelectron spectroscopy at the MAX IV Laboratory
S. Zhu, M. Scardamaglia, J. Kundsen, R. Sankari, H. Tarawneh, R. Temperton, L. Pickworth, F. Cavalca, C. Wang, H. Tissot, J. Weissenrieder, B. Hagman, J. Gustafson, S. Kaya, F. Lindgren, I. Källquist, J. Maibach, M. Hahlin, V. Boix, T. Gallo, F. Rehman, G. D'Acunto, J. Schnadt and A. Shavorskiy
J. Synchrotron Rad. **28** (2021), 624-636.

Abstract

CO_2 chemistry has received significant interest in recent time, due to the greenhouse effects of CO_2 emissions and the resulting climate change. CO_2 reduction reactions, such as methanol synthesis and reverse water-gas shift, is providing a route for recycling of CO_2 and thus limiting the CO_2 emissions. These reactions are commonly performed over Cu-based catalysts, making the interaction of CO_2 and Cu on the atomic scale of tremendous importance for a fundamental understanding and, as a consequence, the development of new and more efficient catalysts.

This thesis presents results on the adsorption and dissociation of CO_2 and initial oxidation of both the low-index Cu(100) and the vicinal Cu(911) surface. Due to the inertness of CO_2, techniques with the possibility to measure at elevated pressures are necessary. Hence, the main methods used in this thesis are Ambient Pressure X-ray Photoelectron Spectroscopy (AP-XPS) and Surface X-Ray Diffraction (SXRD).

It was found that the oxidation of Cu(100) starts by forming a p(2×2) structure that transforms to a p($2\sqrt{2} \times \sqrt{2}$)R45° missing row structure as the oxygen coverage increases. The core-level shifts of the O 1*s* core-level is shown to be a fingerprint of the Cu coordination number of the absorbed oxygen. The results on the adsorption of CO_2 on Cu(100) showed that the increase of oxygen coverage from CO_2 dissociation is constant in the range of 0-0.25 ML (MonoLayers, 1 ML = 1.53×10^{15} cm^{-2}). After 0.25 ML the dissociation is still constant, but with a lower dissociation rate, until the oxygen coverage saturates at 0.50 ML. Results from DFT calculations show that CO_2 dissociation on terraces cannot explain the constant dissociation rate as the adsorbed oxygen drastically affects the stability of adsorbed CO_2. However, steps were found to both lower the dissociation barrier and separate the products, lowering the probability for recombination. Furthermore, the active site was kept available by oxygen diffusion away from the steps, leading to a constant number of reaction sites. Thus, the inclusion of atomic steps on Cu(100) is necessary to explain the experimental findings.

To validate the findings from Cu(100), the vicinal Cu(911), which has closed packed (111) steps each 11.5 Å, was investigated. It was found that the initial oxidation of the surface proceeds by faceting into (410), (401), and (100) facets. As a consequence the steps will reform from being closed packed to the more open (110) steps. As Cu_2O starts to grow on the surface the (410) and (401) facets disappear. Instead the (911), (311), and (100) facets are present.

Well ordered oxide is seen to grow on the (311) facets with the orientation of $Cu_2O(110)$ || Cu(311). The results on the adsorption of CO_2 on Cu(911) show that although the stepped surface facilitate the adsorption, the rate of the increase of atomic oxygen is not faster compared to on Cu(100). This is most likely due to the short terraces where recombination of CO and O takes place more readily. The (110) steps is showed to be able to adsorb CO_2 even with the presence of oxygen, hence showing the importance of the (110) steps for the reaction.

Populärvetenskaplig sammanfattning

Med användandet av fossila bränslen har CO_2-koncentrationen ökat kraftigt i atmosfären, vilket i sin tur leder till problem som klimatförändringar. På grund av dessa klimatförändringar har en önskan att gå över till en kolneutral samhälle ökat kraftigt.

En del av lösningen är att återvinna kolet i CO_2 genom att omvandla CO_2 till mer värdefulla kemiska ämnen, som metanol. Detta kan göras på industriell nivå genom användning av katalysatorer - ett ämne som påskyndar kemiska processer utan att själv konsumeras. Egenskaperna för den nuvarande katalysatorn som används, $Cu/ZnO/Al_3O_2$, är inte tillräckligt tillfredställande för att göra processen ekonomisk lönsam. Detta gör att nya katalysatorer behöver utvecklas för att realisera metanolproduktion på industriell nivå.

En fundamental förståelse av ytreaktionerna på katalysatorn är till hjälp för utvecklingen av nya katalysatorer. Detta kan åstadkommas genom studier av förenklade modellsystem av de relevanta ytorna. I denna avhandling används speciella ytstrukturer av Cu, kallade Cu(100) och Cu(911), som modellsystem för att studera oxideringen av ytorna samt dissociationen av CO_2 till CO och O på ytorna, ett första steg mot produktion av t.ex. metanol.

När en CO_2-molekyl adsorberar (fastnar) på Cu-ytan så kan den dissocieras till CO och O. Eftersom CO binder löst till Cu-ytan så kommer den att desorbera (lossnar) från ytan och resultatet blir att atomärt syre blir kvar på ytan. Resultat från experiment och beräkningar visar att när mängden syre på Cu(100) ytan ökar kommer det ske en övergång mellan två olika strukturer. Ett skift i bindningsenergin från O 1s-elektroner observeras från mätningar när syretäckningsgraden ökar, vilket förklaras med hjälp av beräkningar att vara övergången mellan de två strukturerna. Mätningar av utvecklingen av syretäckningsgraden från CO_2 dissociationen visar att hastigheten för CO_2 dissociation är oberoende av syretäckningsgraden. Beräkningar visar att detta bäst förklaras med att CO_2 dissocierar på de atoma stegen, i stället för på terrasserna.

För att bekräfta att CO_2 dissocierar på de atoma stegen studerars Cu(911), vilket har ett atomärt steg för varje 1.15 nm. Exeriment visar att oxideringen av ytan börjar med att ytan facetterar så att de atomära stegen blir mer öppna. När bulkoxid börjar växa på ytan så försvinner dessa facetter. Mätningar av CO_2 växelverkar med ytan visar att CO_2, till skillnad från Cu(100), kan adsorbera på den syretäckta ytan. Detta visar att de mer öppna stegen är viktiga för att CO_2 skall kunna adsorbera.

Acknowledgements

Foremost, I would like to thank my main supervisor, Johan Gustafson, for the guidance, encouragement, and discussion he has provided during my work.

I would also like to thank my co-supervisor, Edvin Lundgren, who have provided valuable discussions, comments, and advice that have helped me throughout my work.

I would like to thank my theoretical collaborators, Alvaro Posada-Borbón and Henrik Grönbeck, for the successful collaboration and the insightful discussion we have had.

I would also thank Andreas Schaefer for providing an excellent discussion, giving valuable insights, and for all the fun we have had during the experiments. I would also like to thank Lindsay Merte who have provided insights and support during my work.

I would also like to thank Patrik Wirgin who helped me with the administrative work and provided interesting discussions in the lunch room. I want to thank Estephania Lira and Jan Knudsen who always helped me when there was trouble in the lab. I also like to acknowledge Kim von Allmen and Helen Edström for their help on the beamtimes. I am grateful for the rest of the members of the division of Synchrotron Radiation Research who have provided a friendly working environment.

I would like to thank my parents, Lars and Dina, which have always encouraged me and raised me with a thirst for new knowledge. I am also grateful for my three sisters, Emma, Jenny, and Sara who have supported me throughout my life. Finally, and most importantly, I would like to thank my better half Soraya for her full hearted support and love.

Dissociative Adsorption of CO_2 on Copper: The Role of Steps

Chapter 1

Introduction

Catalysis has become an essential part of the modern economy as more than 85% of all chemicals produced have been in contact with a catalyst [1]. In addition, an important application in catalysis is the recycling and conversion of CO_2 into liquid fuels, such as methanol [2]. This process could be essential for society to become carbon neutral and rely on renewable energy, which is critical to counter global warming.

The development of new and more efficient catalysts is of crucial importance. This is especially true for recycling CO_2 into methanol, which could be aided by developing a fundamental understanding of the relevant chemical reactions on the atomic scale, i.e., a knowledge-driven development.

A powerful method to achieve a fundamental understanding of chemical reactions is the surface science approach, which simplifies both the relevant material and conditions. A real catalyst usually consists of a combination of materials such that it becomes difficult to have an atomistic understanding of the processes on the surface. Traditionally, surface science uses single-crystal samples for which the surface under investigation is well-defined and understood in detail, making it easier to get an atomistic understanding of the reactions on the surface. Surface science also typically simplifies the conditions by using ultra-high vacuum and controlled gas dosing, giving a more controlled and suitable environment for the experiments.

Cu-based catalysts play an important industrial role in the reverse water-gas shift and methanol formation; thus, an understanding of the interaction of Cu and CO_2 is desirable. In this thesis, the dissociative adsorption of CO_2 and subsequent oxidation on Cu(100) and Cu(911), which consist of (100) terraces

separated by (111) steps every 11.5 Å, have been studied. In addition, the pure oxidation of these two surfaces has also been studied to understand the structures present under the reaction. The system of interest has been studied using Ambient Pressure X-ray Photoelectron Spectroscopy (APXPS) and Surface X-ray Diffraction (SXRD), complemented by Density Functional Theory (DFT), Low Energy Electron Diffraction (LEED) and Scanning Tunneling Microscopy (STM).

It was found from DFT and XPS that the oxidation of Cu(100) proceeds from a p(2×2) with 0.25 ML of oxygen coverage to the missing row structure with 0.50 ML of oxygen coverage. Core-level shift calculations of the different structures show that the binding energy of the O 1s peak can be used as a fingerprint of the Cu coordination number of the oxygen atoms. The oxygen coverage increase from CO_2 dissociation was measured to have a constant rate in the range of 0-0.25 ML and 0.25-0.45 ML. At 0.25 ML, we found that the rate decreased, and at 0.45 ML, the oxygen coverage started to saturate. From the evolution of the oxygen coverage and DFT calculations, it was found that this behavior could not be explained by CO_2 dissociation on the terraces alone, as the terraces become poisoned by the oxygen adsorption, contradicting the constant rate. Instead, a model in which the CO_2 molecule dissociates at the step is proposed. If steps and oxygen diffusion are included in the model, the constant rate of the oxygen coverage could be explained. The result shows the importance of steps in lowering dissociation barriers and their role in separating products by diffusion to inhibit recombination.

To validate the hypothesis that steps are the active sites for CO_2 dissociation, the vicinal Cu(911) surface was studied. It was found with SXRD that the oxidation of the surface proceeds by faceting into (410), (401), and (100). As a consequence the surface will be transformed from having the closed packed (111) steps to the more open (110) steps. These facets where stable in the parameter range of T=RT-400 °C and p=10^{-10}-10^{-5} mbar O_2, however above 10^{-5} mbar Cu_2O was observed. As the oxide grows the (410) and (401) facets disappear and the surface consists of (911), (311), and (100) facets instead. A well ordered oxide is found on the surface that is oriented with respect to the substrate as $Cu_2O(110)$ || Cu(311). The behaviour of the CO_2 interaction with Cu(911) was different compared to Cu(100). Initially, the CO_2 adsorbed on the surface with no sign of adsorbed atomic oxygen. However, as the adsorbed oxygen start to grow on the surface the adsorbed CO_2 starts to gradually decrease. This continues until the adsorbed oxygen coverage starts to saturate, where the CO_2 adsorption is enabled again. These results show that CO_2 can adsorb on a surface with (110) steps, even in the presence of oxygen. The result, both from

Cu(100) and Cu(911), can be used to develop models for the dissociation of CO_2, which is important in understanding CO_2 reduction in general.

Chapter 2

Catalysis

As mentioned in the introduction, this thesis aims to understand the catalytic reactions better, to further the development of new catalysts. Hence, it is helpful to describe essential features of catalysis and the chemistry involved. However, this thesis only deals with specific steps within the catalytic reaction and the oxidation of the catalyst's surface.

1 Catalysis

In 1835 Jöns Jacob Berzelius coined the term catalysis after investigating several previous experimental observation and concluding that [3],

"It is then shown that several simple and compound bodies soluble and insoluble, have the property of exerting on other bodies an action very different from chemical affinity. The body effecting the changes does not take part in the reaction and remains unaltered through the reaction... I will therefore call it the 'Catalytic Force' and I will call 'Catalysis' the decomposition of bodies by this force,"

However, later on in 1877, G. Lemoine observed that a catalyst could change the reaction rate with which equilibrium is reached, but not the position of the equilibrium itself [4–6]. Thus, catalysis is the process that accelerates a chemical reaction without being consumed.

Typically, catalysis is divided into two main categories depending on which phase the catalyst and reactants are found. These two categories are heterogen-

eous catalysis, in which the catalyst and the reactants are in different phases, and homogeneous catalysis, in which the catalyst is in the same phase as the reactants. This thesis will only deal with heterogeneous catalysis, in which the catalyst is a solid surface and the reactants and products are in gas phase.

Figure 2.1 illustrates how a heterogeneous catalyst accelerates the chemical reaction $A + B \rightarrow C$ by considering the potential energy diagram of the catalyzed and non-catalyzed reactions. The non-catalyzed reaction, i.e., the reaction in the gas phase, can occur; however, the energy barrier to overcome, and as a consequence forming the product, is extensive. On the other hand, the catalyzed reaction gives an alternative and more complex reaction path by first bonding the reactants to the catalyst, after which the reaction to the product proceeds. The activation barrier for the formation of the product is much lower than in the gas phase, hence, making the reaction faster. In the last step, the product desorbs from the catalyst, which is also associated with an energy barrier, returning the catalyst to the initial state. It should be noted that the overall free energy does not change for the catalyzed reaction, meaning that the equilibrium constants are the same for both reaction pathways [7]. This means that if a reaction is thermodynamically unfavorable, the catalyzed reaction will also be thermodynamically unfavorable.

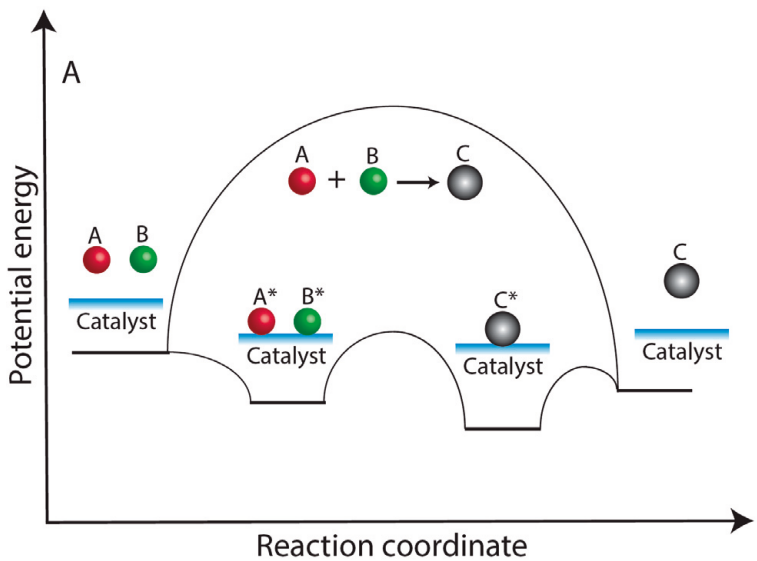

Figure 2.1: Potential energy diagram illustrating the concept of a heterogenous catalytic reaction. The non-catalyzed reaction is associated with larger barrier to form the product. For the catalyzed reaction the reactants can bind to the catalyst after which the products can form with an smaller associated barrier. The catalyst will return to its original state after the product desorb from the catalyst.

As illustrated above, the catalyst works by breaking and forming new chemical bonds [8]. What typically makes the reaction faster is that the catalyst makes it easier to break strong bonds. This is the case for the reaction in this thesis, where the breaking of the C-O bond in the gas phase CO_2 molecule has an energy barrier of about 3 eV, but as shown in Paper II, if a Cu surface is introduced the energy barrier can decrease to around 0.5 eV.

2 CO_2 chemistry

As mentioned in the introduction, CO_2 chemistry, especially the recycling of CO_2, is vital for reducing greenhouse gases in the atmosphere. However, CO_2 is a quite inert molecule and challenging to reduce and convert into more desirable products. The catalytic reduction of CO_2 by hydrogenation with H2 can lead to various products, such as (1) CO, which is produced with the reverse water gas shift reaction (RWGS), (2) methanol, and (3) methane:

$$
\begin{aligned}
&(1)\ CO_2 + H_2 \rightleftharpoons CO + H_2O \\
&(2)\ CO_2 + 3H_2 \rightleftharpoons CH_3OH + H_2O \\
&(3)\ CO_2 + 4H_2 \rightleftharpoons CH_4 + 2H_2O
\end{aligned}
$$

However, methanol is the most desirable product, as it can be used as a liquid fuel and is a more important chemical feedstock, thus giving the most attention [9].

$Cu/ZnO/Al_2O_3$ is used as a catalyst for methanol production on an industrial scale, with a gas mixture of $CO_2/CO/H_2$ [10]. Isotope-labeling experiments show that the carbon in the resulting methanol comes from CO_2. But, there are several problems with the current catalyst used for CO_2 hydrogenation to methanol. The by-product of water from methanol formation and RWGS have been shown to deactivate the catalyst [11]. There is also a selectivity issue as RWGS takes place over the same catalyst, consuming H_2 and producing water and CO [12]. Surface oxidation of the Cu has been seen to deactivate CO_2 adsorption, explaining the need for CO in the gas mixture [13]. Additionally, several other products, such as hydrocarbons and higher alcohols, are typically associated with methanol synthesis, giving further problems with selectivity.

Thermodynamically, methanol formation from CO_2 hydrogenation is exothermic and is favorable at higher pressures and lower temperatures [14]. However, due

to the inertness of CO_2 and the temperature dependence of the reaction rate, higher temperatures (>500 K) will facilitate the reaction. Higher temperatures will also make the RWGS more favorable, which will consume hydrogen and reduce the methanol formation.

The favorable thermodynamics, low product yields, and selectivity suggest that the issue is the surface reactivity of the catalyst [12]. A deeper understanding of the fundamental reaction steps on the surface would provide valuable information for the design of better catalysts with more desirable properties.

3 Kinetics

Kinetics describes the rate at which a chemical reaction occurs and correlates the rate to a reaction mechanism. Thus, kinesics has been a key discipline for catalysis, as it gives a framework for relating macroscopic and microscopic properties [7].

Consider the following elementary reaction where the reactants A and B form the products C and D,

$$\nu_a \mathrm{A} + \nu_b \mathrm{B} \longrightarrow \nu_c \mathrm{C} + \nu_d \mathrm{D},$$

where ν_a, ν_b, ν_c, and ν_d are the stoichiometric constants. The rate of the reaction can be expressed as the decrease of the reactants A or B or the increase of the products C or D over time,

$$r = -\frac{1}{\nu_a}\frac{d[A]}{dt} = -\frac{1}{\nu_b}\frac{d[B]}{dt} = \frac{1}{\nu_c}\frac{d[C]}{dt} = \frac{1}{\nu_d}\frac{d[D]}{dt}$$

where [X] is the concentration of the species X. With the use of the rate constant k, which describes the speed of the reaction, the rate can be expressed with the use of the power rate law

$$r = k[A]^a[B]^b,$$

where a+b gives the order of reaction. The order of the reaction describes how the rate changes with the concentration of the reactants. For a first-order reaction the rate of reaction is proportional to the concentration of one substance

and for a second-order reaction the rate is dependent on the concentration of two substances. To derive the change of the concentration of a species over time the rate law has to be integrated. This is easy for the first-order reaction

$$A \xrightarrow{\mathrm{k}} B + C,$$

where A dissociates into B and C. Here, the rate can be expressed as

$$r = k[A] = -\frac{d[A]}{dt}$$

By integrating the above rate equation, one gets the expression of the time-dependent concentration of reactants and products:

$$[A] = [A]_0 e^{-kt}, [B] = [C] = [A]_0(1 - e^{-kt})$$

Thus, for the above reaction, the reactant decays exponentially with time. The change of the concentrations is illustrated in Figure 2.2.

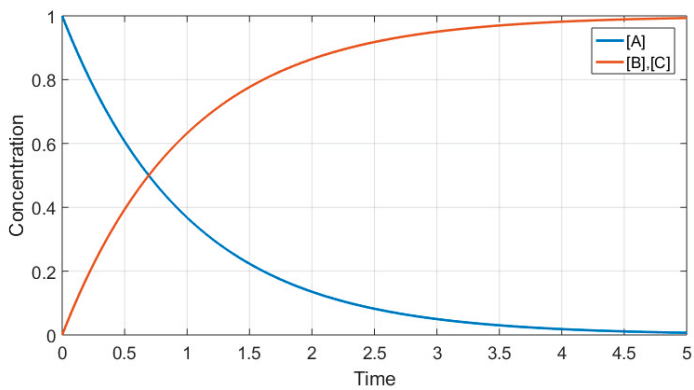

Figure 2.2: Evolution of [A], [B], and [C] in the first order reaction $A \xrightarrow{\mathrm{k}} B + C$,.

The temperature and activation barrier dependence of the rate constant for an elementary reaction step, like the dissociation of a molecule, is given by an empirically derived equation called the Arrhenius equation

$$k(T) = \nu e^{-E_a/k_b T},$$

where ν is a pre-exponential factor and E_a the activation energy. The physical interpretation of the Arrhenius equation is seen in Figure 2.3, where a potential barrier with a height of E_a has to be overcome for the reaction to happen. The exponential behavior can be realized by integrating all values larger than E_a in the Maxwell-Boltzmann distribution - the distribution of kinetic energies in gas-phase molecules - which is proportional to e^{-E_a/k_bT}.

The pre-exponential factor is sometimes referred to the "frequency-factor," as it can be interpreted as the frequency of collisions. This can be seen by having no activation energy requirements, by having E_a=0, in which case k(T)=ν. In this situation, the limiting factor would be the frequency of events that could lead to a reaction. By using frameworks as the Collision Theory, in which the reactants are treated as Billiard balls, or Transition State Theory, where the vibrational and rotational energies of the molecules are taken into account, the pre-exponential factor will have a temperature dependence. However, the temperature dependence of the pre-exponential term tends to be much weaker than the exponential term and is therefore usually neglected [7].

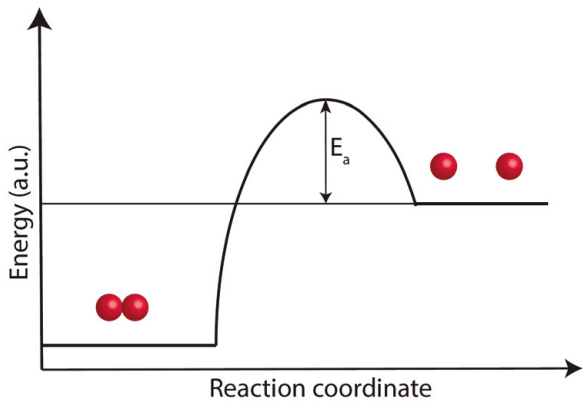

Figure 2.3: Illustration of the energy diagram of the dissociation of a molecule.

The Arrhenius equation gives a framework for understanding the effect of temperature and activation energies on the rate of a chemical reaction. Specifically, it shows that reaction pathways with significantly lower activation energy will dominate and control the overall reaction rate. Thus, less occurring sites can control the reaction rate if the activation energy is considerably lower than the more occurring reaction sites. An example of this is shown in paper II, where the atomic steps on Cu(100) are shown to control the dissociation of CO_2.

Chapter 3

Crystal and Surface Structure

Most materials are crystalline, which means that there is an order in the internal atomic arrangement in the material. The relevant materials for this thesis, Cu and Cu_2O, are crystalline, and hence the description of their crystalline properties is essential. In the following section, concepts such as crystal lattices, reciprocal lattice, surface structures, thermodynamics of surfaces, and adsorption will be described.

1 Crystal lattices

A crystal consists of periodically arranged atoms or groups of atoms; hence, it can be described by a Bravais lattice. The Bravais lattice consists of an array of points in space, ordered such that any lattice vector,

$$\mathbf{R} = n_1\mathbf{a}_1 + n_2\mathbf{a}_2 + n_3\mathbf{a}_3, \text{where } n_1,\ n_2, \text{ and } n_3 \in \mathbb{Z},$$

connects two equivalent points in the lattice [15]. $\mathbf{a}_1$, $\mathbf{a}_2$, and $\mathbf{a}_3$ are the basis vectors that define the Bravais lattice. Each lattice point in the Bravais lattice contains one or several atoms forming a base, which, together with the basis vectors, defines the entire crystal structure.

As the crystal is periodic, it is enough to describe a so-called unit cell, which will build up the entire crystal when translated for a subset of $\mathbf{R}$. The smallest possible unit cell is called the primitive unit cell; however, due to convenience often a larger unit cell is used to describe the crystal.

The unit cells of the relevant materials for this thesis, Cu and Cu_2O, can be seen in Figure 3.1. Cu is described with a cubic unit cell, where the atoms are positioned at the corners and faces of the cube, called Face Center Cubic (FCC). Cu_2O is also described with a cubic unit cell, but with the oxygen positioned as Body Center Cubic (atoms at the corners and in the center) sublattice and Cu as an FCC sublattice, but shifted by a quarter of the cube diagonal. With this description, the Cu unit cell will have a basis with four atoms and the Cu_2O unit cell with six atoms, four Cu atoms and two O atoms.

The size of the unit cell in the crystal is described by the lattice constant, which in the case of the cubic unit cells is the height of the cell (see Figure 3.1). For Cu and Cu_2O, the lattice constants are $a_{Cu} \approx 3.6$ Å and $a_{Cu2O} \approx 4.3$ Å respectively.

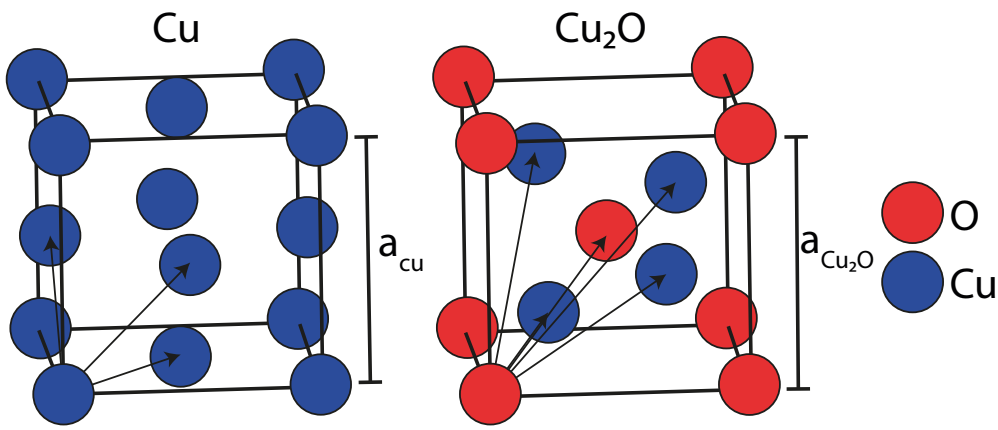

Figure 3.1: The Cu and Cu_2O crystal lattices. The black lines indicate the unit cell while the black arrows indicate the base of the unit cell. The lattice constants of Cu and Cu_2O are indicated in the figures with a_{Cu} and a_{Cu2O}. Note that the two unit cells are not in the same scale as $a_{Cu} \approx 3.6$ Å and $a_{Cu2O} \approx 4.3$ Å.

2 Reciprocal lattice

A useful concept connected to the Bravais lattice is its reciprocal lattice, which is defined as

$$\mathbf{G} = h\mathbf{b}_1 + k\mathbf{b}_2 + l\mathbf{b}_3,\ h, k \text{ and } l \in \mathbb{Z},$$

where the vectors $\mathbf{b}_1$, $\mathbf{b}_2$, and $\mathbf{b}_3$ are defined as

$$\mathbf{b}_i \cdot \mathbf{a}_j = \delta_{ij} 2\pi.$$

From the above equation it is straightforward to construct the reciprocal lattice if the corresponding real space lattice is known, and visa versa. It should be noted from the above equation that

$$|\mathbf{b}_i| \propto \frac{1}{|\mathbf{a}_i|},$$

thus larger distances in real space will give smaller distances in reciprocal space, and visa versa. An important property of the reciprocal lattice of 2D lattices is that the symmetry remains from the transformation to the reciprocal lattice, e.g., a hexagonal pattern in real space will also be hexagonal in reciprocal space. The reciprocal lattice is of great importance for diffraction studies, as will be discussed further in chapter 4.3.

3 Surfaces

The description above is of an infinite 3D crystal, but in reality, the crystal is always finite, exposing some kind of surface or interface to the surrounding. These interfaces, between the solid material and liquid/gas, are interesting because the electronic structure will be different on the interface compared to the bulk. As a consequence, the chemical properties are different on the surface as compared to the bulk. Moreover, several important phenomena and processes occur on surfaces, such as the chemical reaction of a heterogeneous catalyst. To understand these chemical reactions, the respective surfaces have to be investigated.

3.1 Single Crystal Surfaces

The work in this thesis has been performed by using model catalysts to better understand the oxidation of the material and the dissociation of CO_2 on the catalyst. The model catalysts consist of well-defined single crystal Cu surfaces, in which the structures of the surface are known, thus making it possible to correlate surface structure and activity.

Single crystals are solids that have their crystal structure unbroken throughout the sample. To create a well-defined surface, the single crystal is cut along

a specific plane. Depending on the plane's orientation relative to the crystal lattice, the surface will have a particular structure. This is illustrated in Figure 3.2, where the FCC crystal is cut along three different crystallographic planes. The orientation of such a plane is described by the so-called Miller indices, which are constructed by the inverse interception points between the plane and the axes of the unit cell, normalized such that all three are as small integers as possible [16].

Figure 3.2 shows three examples of Miller indices (100), (110), and (111), which are usually referred to as low-index surfaces. In 3.2(a), the plane intersects the x-axis at 1 but is parallel to the y-and z-axis, in (b), the plane intersects the x-and y-axis at 1 but is parallel to the z-axis, and in (c), the plane intersects all the axes at 1. When the plane is parallel to an axis, the plane and axis will never intersect; thus, the intersection is said to be at ∞ and its reciprocal value 0. Hence, the intersection points will be $(1\infty\infty)$, (11∞), and (111), and the reciprocal values, and the corresponding Miller indices, then becomes (100), (110), and (111).

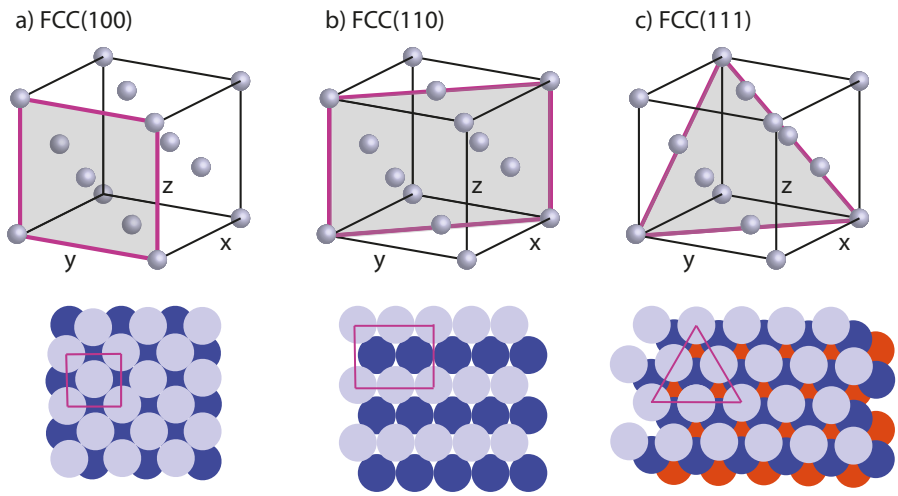

Figure 3.2: (a)-(c) shows the (100), (110), and (111) surface structures of FC crystals.

The 2D Bravais lattice that describe the surface structure is defined in a similar manner as the 3D Bravais lattices, but with only 2 basis vectors $\mathbf{a}_1$ and $\mathbf{a}_2$,

$$\mathbf{R} = n_1\mathbf{a}_1 + n_2\mathbf{a}_2, \text{where } n_1 \text{ and } n_2 \in \mathbb{Z},$$

Steps and vicinal surfaces

Real samples do not consist of infinite perfectly flat surfaces, but instead, the surface consists of flat terraces separated by steps (see Figure 3.3). As the step atoms will miss neighboring atoms, the step atoms will be physically and chemically different from terrace atoms. Thus, to get a complete understanding of the catalytic properties of a surface, the steps have to be taken into account. Additionally, there might be different types of steps on the surface, as illustrated in Figure 3.3, providing additional complications of the model system.

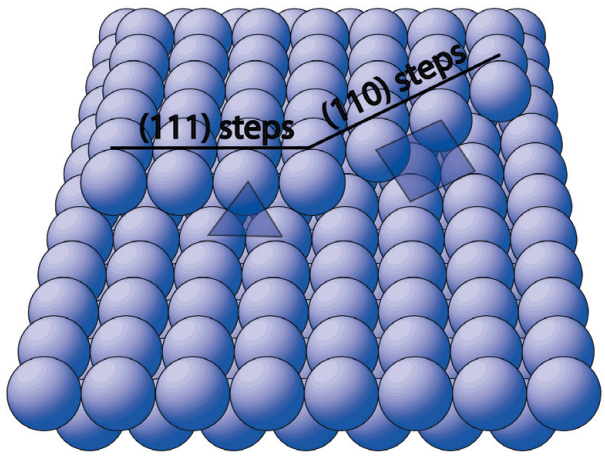

Figure 3.3: The two types of steps on a FC(100) surface. The triangle and rectangle indicate the (111) and (110) micro facets, respectively.

The most closed-packed steps on an FCC(100) surface are the (111) steps, which are oriented in the [011] or [$0\bar{1}1$] directions. The (111) steps form (111) micro facets, thus its name (111), on the surface, which can be seen by the triangle in Figure 3.3. Steps can also be oriented in the [010] or [001] direction forming (110) steps, as illustrated with the rectangle in Figure 3.3. The (111) and (110) steps are usually referred to closed and open steps, respectively, as the atoms lie in the closed packed (111) configuration or the more open (110) configuration.

The atoms in the open (110) steps are less coordinated than in the closed (111) steps, making it natural for the (111) steps to be more stable. On Cu(100), the (111) steps should be expected to dominate as the formation energy of (111) steps is lower than of the (110) steps [17]. However, the entropy of the dense (111) steps is lower than for steps with other orientations, making the (111) steps less favorable at higher temperatures [18]. The relative stability of (110) and (111) steps can change by adsorption of molecules or atoms, and the (110)

steps will be preferable on an oxygen-covered surface, as seen in Paper III.

For any study involving steps, the closed-packed surfaces are not ideal as the step density varies depending on sample quality and preparation. For any systematic investigation, vicinal surfaces have to be used instead. These vicinal surfaces are cut at an angle close to the low-indexed surfaces, hence its name "vicinal," creating terraces with the corresponding low-indexed surface separated with a monatomic step. These vicinal surfaces, such as (m,1,1) where m$\leq$2, are a more fitting candidate for model systems involving step sites as the step density is controlled.

Examples of two vicinal surfaces used in the thesis are seen in Figure 3.4. These surfaces consist of (100) terraces separated by (111) steps, where (911) has a 4.5 atoms wide terrace and (611) has a terrace width varying between 2.5 and 3.5 atoms.

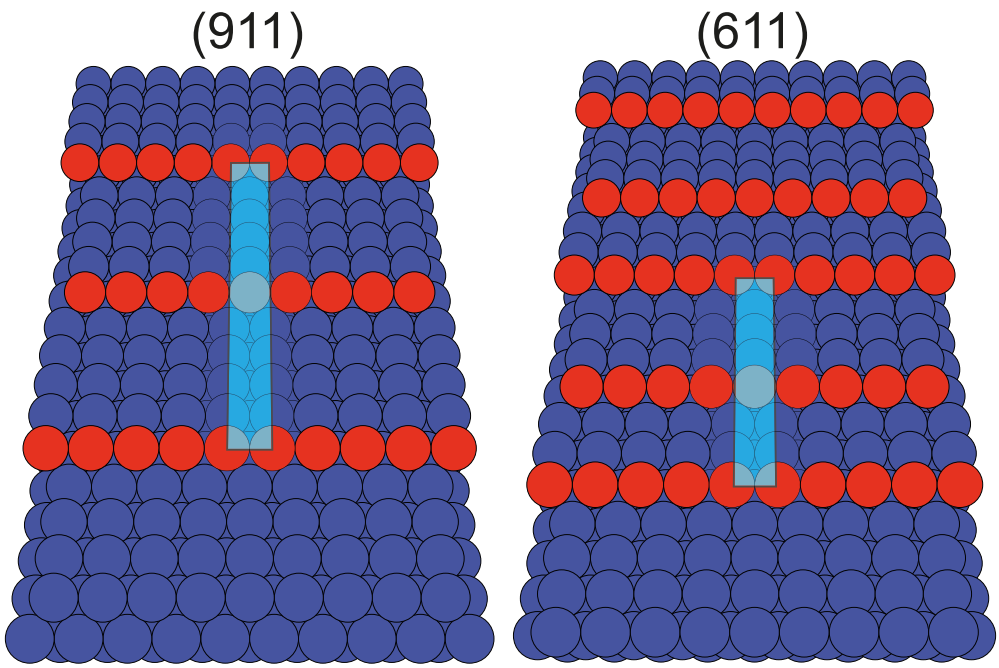

Figure 3.4: (911) and (611) vicinal surfaces of FCC. The red circles indicate the step atoms and the shaded rectangle the unit cell of the surface.

3.2 Surface Structures

Depending on the Miller indices of the surface, different surface structures with different physical and chemical properties will be created. This is apparent for CO_2 adsorption on Cu surfaces where the reactivity follows the trend Cu(110) > Cu(100) > Cu(111) [19–22]. For many materials, the surface structure is bulk terminated with only slight changes, such as out-of-plane relaxations of the atoms at the surface. However, the surface can reconstruct, changing the surface structure to compensate for the broken bonds created by the termination of the bulk structure [23]. Foreign atoms or molecules can adsorb on the surface, forming an ordered overlayer or reconstruct the surface, again changing the physical and chemical properties of the surface. Thus, it is essential to know the structure of the surface being studied to gain a fundamental understanding of the surface reactivity.

The unit cell of the surface structure is usually expressed in terms of the bulk terminated unit cell, that is as it would be if there was no reconstruction. Wood's notation is commonly used to describe the new surface structure, and is defined as

$$q\left(\frac{|\mathbf{a}_1^{'}|}{|\mathbf{a}_1|}\times\frac{|\mathbf{a}_2^{'}|}{|\mathbf{a}_2|}\right)R\Theta - A$$

where $\mathbf{a}_1^{'}$, $\mathbf{a}_2^{'}$, $\mathbf{a}_1$, and $\mathbf{a}_2$ the basis vectors of the overlayer/surface reconstruction and the substrate, respectively. $R\Theta$ is the angle between the basis vectors of the overlayer and the substrate. q is either p of c depending on if the overlayer unit cell is primitive or defined such that a Bravais lattice point exists in its center and A defines the adsorbates on the surface.

Figure 3.5 shows the Cu(100) surface as well as two examples of overlayer structures created by oxygen adsorption on Cu(100). The first example, in Figure 3.5b, shows the $p(2\times 2)$ structure on Cu(100) where the unit cell of the oxygen structure is twice as large as the substrate. The second example, in Figure 3.5c, show the missing row (MR) structure which has a $\mathrm{p}(2\sqrt{2}\times\sqrt{2})\mathrm{R}45^\circ$ overlayer structure compared to the substrate. In the MR structure every fourth row of Cu atoms in the [001] or [010] directions have been ejected from the surface creating "missing" rows of Cu atoms. As a result of the reconstruction, the O atoms are coordinated to three instead of four Cu atoms.

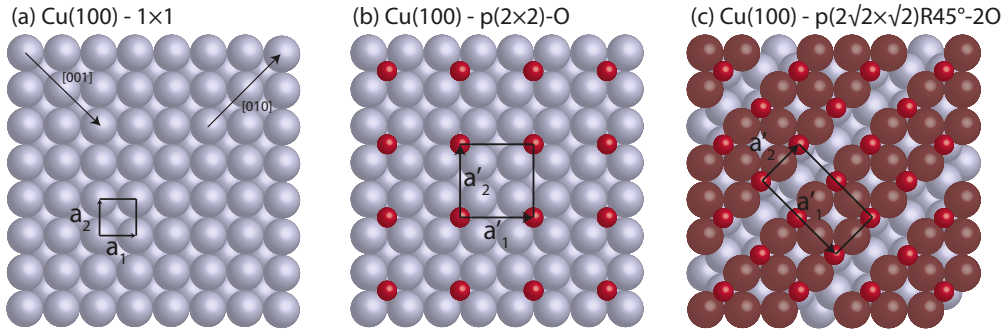

Figure 3.5: **(a) the structure of the pristine Cu(100) surface, (b) the Cu(100)-p(2×2)-O structure, and (c) the Cu(100)-p(2$\sqrt{2}$ × $\sqrt{2}$)R45°-2O structure. The black squares and rectangle show the unit cell of the respective surfaces.**

Faceting

It is common that vicinal surfaces undergo structural changes by faceting to minimize their surface free energy. Faceting consists of reforming the surface to two or more facets, which could spontaneously happen on the clean surface or be adsorption induced. A requirement is that the average orientation of the surface remains the same. Faceting inevitably leads to a higher surface area; hence it is not necessary that a vicinal surface would facet into the more stable low-indexed surfaces as it would also increase the surface area and as a consequence increasing the energy. Figure 3.6 illustrates the faceting of a surface into two additional facets.

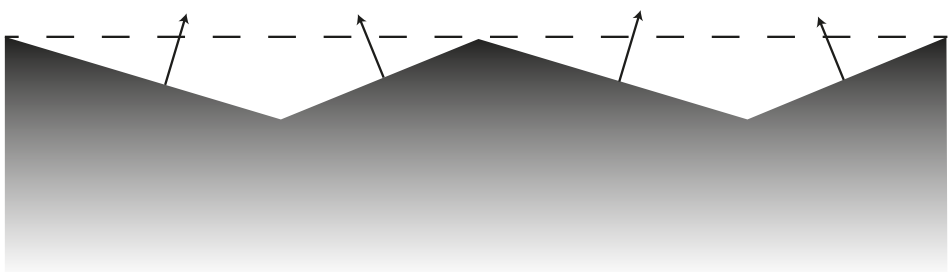

Figure 3.6: Illustration of faceted surface. The original surface is shown as the dashed line. The overall direction of the new surface is the same as the un-faceted surface.

For Cu(911), which is studied in Paper III-IV, faceting to (410) and (401) takes place under the initial oxidation of the surface. However, as the overall orient-

ation of the surface has to remain as (911), larger (100) facets has also to be present.

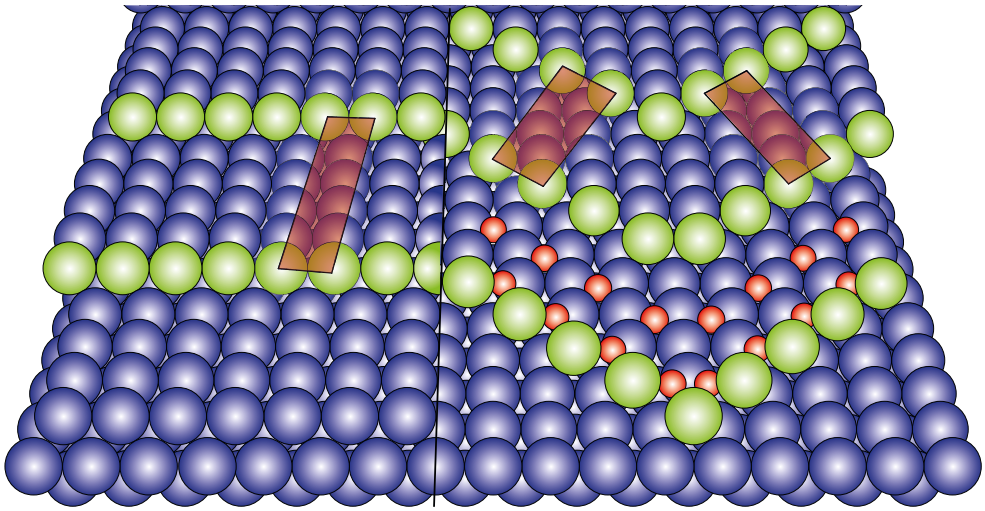

Figure 3.7: Model of the Cu(911) (left) and the faceted Cu(911) surface (right). Faceting of (911) will yield (410) and (401), which have (110) steps instead of (111). The turquoise atoms indicate the step atoms and the red atoms indicate the oxygen atoms on the 410) and (401) facets. The rectangles show the unit cells of the respective surfaces.

Thermodynamics of Surfaces

As mentioned above, the knowledge of the surface structure under reaction conditions is crucial for an atomistic understanding of chemical reactions on a surface. Thus, it is of importance to understand which surface structures are present and how they evolve. The thermodynamics of surfaces give us an insight into the structures present.

Forming a surface on a crystal costs energy due to the broken bonds of the surface atoms compared to bulk atoms. The surface free energy, γ, is defined as the excess free energy of the surface, compared to the bulk, per unit area [24]. The stability of a surface structure will then be given by its surface free energy as the system will be driven to minimize its total energy by forming the most stable surface structure.

The surface free energy can be lowered by forming new bonds by either surface reconstruction or by adsorption. The surface free energy can also be reduced by faceting; however, this will lead to an increase in the surface area and, as a consequence, an increase in energy. However, the higher surface area can be

compensated by a facet with a significantly lower surface free energy, decreasing the total free energy of the surface.

For a specific chemical potential, the expected structure is the structure that minimizes the surface free energy. By plotting the surface free energy, which can be calculated from DFT, of the different structures, creating a surface stability plot, it becomes straightforward to see what structures should be present on the surface. This is illustrated in Figure 3.8, where the free energy of three hypothetical structures is shown. The shaded regions show under which conditions the different structures are expected to exist.

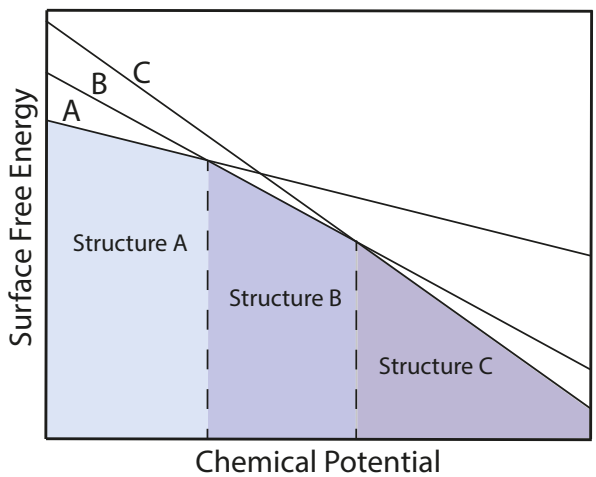

Figure 3.8: Illustration of the surface free energy of three different structures at different chemical potentials.

In paper I, the stability plot was used to examining how the surface structure evolved as the oxygen coverage increased, see Figure 3.9. This is done by looking at the structure with the lowest free energy as the chemical potential increase, meaning that the surface structure in Figure 3.8 should evolve as pristine Cu(100)→p(2×2)→MR as the oxygen chemical potential increases. Only one of the structures is the most thermodynamically stable, and should be observed on the surface in the end. However, due to limitation in the kinetics, it takes time to adsorb enough oxygen to form the MR structure, the p(2×2) will also be observed on the surface.

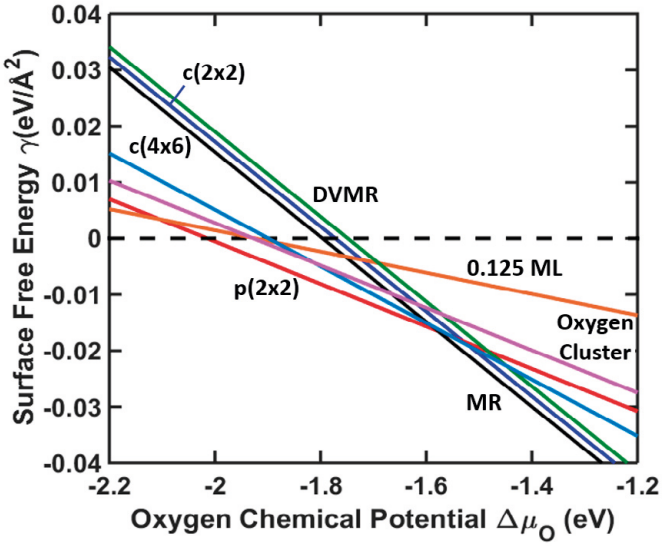

Figure 3.9: Calculated surface free energy vs. oxygen chemical potential of 7 different O/Cu structures. The surface free energies are calculated relative to the pristine Cu(100) surface. The Figure is taken from Paper I.

Copper oxide formation

If copper is exposed to oxygen, adsorbed oxygen will start to appear on the surface. For the case of Cu(100), structures as shown in Figure 3.5(b) and (c) starts to form. However, as the surface is exposed to enough oxygen for longer times, an oxide is expected to appear. At oxygen pressures and temperatures used in this thesis only cuprous oxide, Cu_2O, is expected to be found [25]. The formation of Cu_2O proceeds via the formation of islands that grow in 3D. Typically, when the material is capable to form uniform oxide layers, the oxide will then grow uniformly, and not via island formation. However, due to the mismatch between the Cu substrate and the Cu_2O oxide, the oxide forms via island formation [25]. At moderate oxygen pressures the growth of Cu_2O on Cu(100) is epitaxial and the orientation of the oxide islands with respect to the substrate is $Cu_2O(100)$ || Cu(100) [26–28]. The oxide islands on Cu(100) will have a (6×7) lattice misfit configuration [29].

In paper IV, Cu_2O was found to grow on Cu(911) with $Cu_2O(110)$ || Cu(311) on Cu(911). The reason for the $Cu_2O(110)$ oxide to be oriented with (311) and not (911) is that the rows of Cu on the oxide surface fits (311), and not (911). The distance between the row of Cu atoms in (911) is ∼11.63 Å and ∼4.23 Å for (311), compared to ∼4.27 Å for $Cu_2O(110)$.

3.3 Adsorption

The adsorption of molecules onto surfaces can be categorized into two main categories, physisorption and chemisorption, depending on the nature of the interaction [18]. For physisorption, the interaction between the surface and adsorbate is weak, and the electronic structure of the adsorbate is only slightly perturbed compared to the gas phase species. The force governing physisorption is the van der Waals force, and the change of enthalpy[1] is generally in the same order of magnitude as for condensation.

If the interaction between the adsorbate and the surface is stronger than physisorption, it is regarded as chemisorption. These interactions typically involve charge transfer between the adsorbate and the surface, creating new chemical bonds. Thus, the change in the electronic structure between the adsorbate and the gas phase species is more significant for the chemisorbed state than in the physisorbed state. This makes it usually easy to distinguish the two different adsorption states in X-ray Photoelectron Spectroscopy (XPS).

Adsorption sites

Molecules or atoms tend to adsorb at preferential sites on the surface, where the adsorbate is stabilized. Adsorbates are often found to be stable at or near sites that are highly symmetrical in the lateral direction. There are three different high-symmetry adsorption sites on an FCC(100) surface, shown in Figure 3.10; (T) Top site, in which the adsorbate stabilize directly above a substrate atom, (H) fourfold hollow site, where the atoms stabilize in the middle of four substrate atoms, and (B) a twofold bridge site, where the adsorbate stabilize in-between two neighboring substrate atoms.

[1] Enthalpy, H, is the internal energy of the system plus the product of the pressure and volume, i.e., H=U+pV. The change of enthalpy, ΔH, which is more useful, is the heat released or consumed by a system from a process if the system is free to expand or contract.

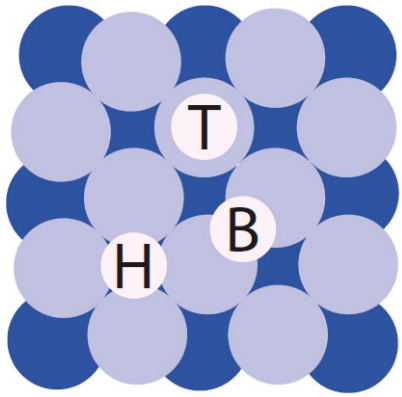

Figure 3.10: Illustration of the different high-symmetry adsorption sites on a FCC(100) surface, where T is the top site, B is the twofold bridge site, and H is the fourfold hollow site.

CO_2 adsorption

Physisorption of CO_2 typically only happens on the surface well below room temperature and the molecule will remain in its linear configuration, as in the gas phase. CO_2 in this state is typically non-reactive, similar to gas phase CO_2 [30]. However, chemisorption of CO_2 as an anionic $CO_2^{-\delta}$ species increases the molecule's reactivity and is considered an essential intermediate state in several systems for dissociation [12]. In this case, there is a charge transfer from the surface to the CO_2 molecule, which results in a bent geometry of the molecule, see Figure 3.11.

The adsorption of CO_2 as $CO_2^{-\delta}$ on a Cu(100) surface is reported in Paper II to be stable, as there is a local energy minimum, but exothermic by 0.4 eV. This makes the equilibrium heavily favorable towards the gas phase CO_2, making the population of $CO_2^{-\delta}$ nondetectable under UHV conditions at RT. However, as the pressure increases, the population of $CO_2^{-\delta}$ on the surface will increase as the number of CO_2 gas molecules impinging on the surface increases, making it possible to detect $CO_2^{-\delta}$ at RT with techniques such as APXPS. This is seen in the supporting information for Paper II, where a $CO_2^{-\delta}$ peak appears at 0.4 mbar at RT.

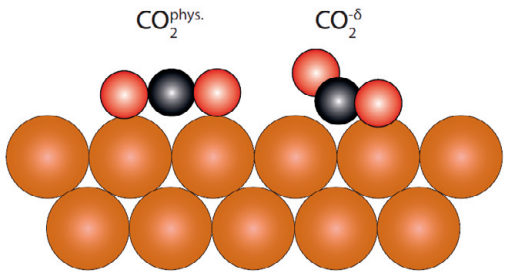

Figure 3.11: Illustration of the difference between the physicorbed CO_2 and the chemisorbed $CO_2^{-\delta}$ molecules.

The reaction of interest in this thesis is the dissociation of CO_2 to CO and O on Cu, where $CO_2^{-\delta}$ is believed to be an intermediate species. CO binds weakly on Cu, and thus it will desorb easily, leaving atomic oxygen adsorbed on the surface [31]. This means that, as the reaction takes place, the oxygen coverage will increase on the surface. The overall reaction

$$CO_2(g) \rightarrow CO(g) + O^*,$$

where (g) and * indicates gas-phase or adsorbed species, respectively, is endothermic by >1 eV. However, we still expect to achieve some oxidation of the Cu surface due to CO_2 dissociation, as the system will be driven to equilibrium. Thos is observed by *ex-situ* experiments by P. B. Rasmussen *et al.* [22]. P. B. Rasmussen's experiments showed that when the Cu(100) sample is exposed to 990 mbar of CO_2 in a closed cell, adsorbed oxygen on the surface will appear. Paper II reports an *in-situ* experiment were the surface is exposed to 0.4 mbar of CO_2 at 100 °C, which leads to an oxidation of the surface similar to what seen in ref. [22].

Chapter 4

Instrumentation and Methods

1 X-ray Diffraction

Since its discovery in 1895 by Wilhelm Conrad Röntgen, X-rays have been a widely used tool for probing materials [32]. Today X-rays are used in various techniques, such as Small-angle X-ray scattering, X-ray tomography, X-ray absorption spectroscopy, etc. In this thesis, X-ray diffraction, specifically Surface X-Ray Diffraction (SXRD), has been used to investigate our system under various conditions. Specifically, SXRD has been used in Paper III and IV to investigate Cu's oxidation. Hence, in the following section, the general theory, concepts, instrumentation, and data analysis will be explained, needed to understand the results.

1.1 General Theory

X-ray diffraction uses the wave-like nature of X-rays, which when scattered from atoms in a material will give a detailed information on the crystalline structure. X-ray diffraction arises from Thompson scattering and as a consequence the incoming and outgoing wave vector has the same magnitude, i.e. $\mid \mathbf{k}_{in} \mid = \mid \mathbf{k}_{out} \mid = \mathrm{k}$. Laue formalism will be used in this thesis to describe X-ray diffraction, which states that the Q vector, i.e the change in wave vector **k**, has to be equal to a reciprocal lattice vector for scattering amplitude to be non-vanishing.

Figure 4.1 illustrates the Laue Condition, where **k** and **k'** are the incoming and outgoing X-rays respectively. **R** is the Bravais lattice vector between the two

scattering points. The path difference Δ is equal to $d + d'$, which can be written as

$$\Delta = d + d' = Rcos(\theta') + Rcos(\theta) = \frac{\mathbf{R} \cdot \mathbf{k'}}{k} - \frac{\mathbf{R} \cdot \mathbf{k}}{k} = \frac{\mathbf{R} \cdot \Delta\mathbf{k}}{k}, \tag{4.1}$$

where k is the length of the k-vectors. For constructive interference, the path difference, Δ, has to be equal to an integer number times the wave-length, i.e.

$$\Delta = n\lambda = n\frac{2\pi}{k}. \tag{4.2}$$

Equation 4.1 and 4.2 can be combined to

$$\mathbf{R} \cdot \Delta\mathbf{k} = 2\pi n.$$

$\Delta\mathbf{k}$ is a reciprocal space vector which can be expressed in the basis vectors of the reciprocal lattice as

$$\Delta\mathbf{k} = h\mathbf{b}_1 + k\mathbf{b}_2 + l\mathbf{b}_3,$$

where h, k, and l can be any number. However, for constructive interference to occur, the vector product between the real lattice vector, $\mathbf{R}$, and $\Delta\mathbf{k}$ have to be equal to $2\pi n$. Thus, we get

$$\mathbf{R} \cdot \Delta\mathbf{k} = (n_1\mathbf{a}_1 + n_2\mathbf{a}_2 + n_3\mathbf{a}_3) \cdot (h\mathbf{b}_1 + k\mathbf{b}_2 + l\mathbf{b}_3) = (n_1h + n_2k + n_3l)2\pi = 2\pi n.$$

From the above equation we get

$$(n_1h + n_2k + n_3l) = n.$$

For the above equation to be true for all real lattice vectors, h, k, and l have to be integers. Hence, $\Delta\mathbf{k}$ has to be a reciprocal lattice vector. On the other hand, the dot product of any reciprocal lattice vector with any real lattice vector $\mathbf{R}$ is equal to

$$\mathbf{R} \cdot \mathbf{G} = (n_1\mathbf{a}_1 + n_2\mathbf{a}_2 + n_3\mathbf{a}_3) \cdot (h\mathbf{b}_1 + k\mathbf{b}_2 + l\mathbf{b}_3) = (n_1h + n_2k + n_3l)2\pi = 2\pi n.$$

So we get

$$(n_1 h + n_2 k + n_3 l) = n.$$

This is fulfilled with $\Delta\mathbf{k} = \mathbf{G}$. Hence, the change in wave-vector $\Delta\mathbf{k}$ has to be equal to a reciprocal lattice vector $\mathbf{G}$ for constructive interference to occur. With this, we have arrived at the Laue condition

$$\Delta\mathbf{k} = \mathbf{G}$$

or

$$\mathbf{Q} = \mathbf{G}$$

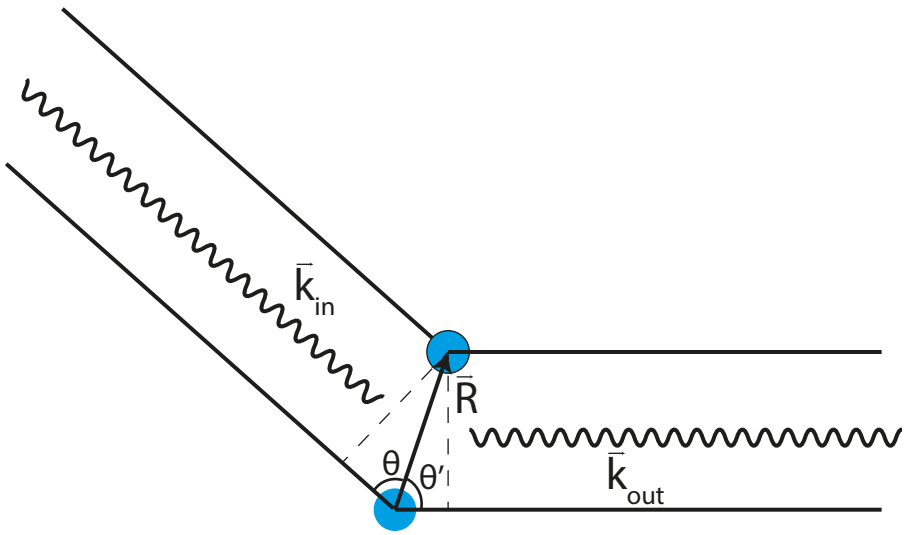

Figure 4.1: Illustration of the Laue condition. The incoming X-rays scatters from two objects separated by **R**.

The scattering amplitude from diffraction of a crystal can be calculated from

$$F^{crystal}(\mathbf{Q}) = \sum_n e^{i\mathbf{Q}\cdot\mathbf{R}_n} \sum_j f_j(\mathbf{Q}) e^{i\mathbf{Q}\cdot\mathbf{r}_j},$$

where the first sum is over all real lattice vectors $\mathbf{R}$, i.e. the lattice sum, and the second is over the basis of atoms associated to each lattice point, called the unit

cell structure factor [32]. When describing a crystal having a monatomic base the second sum reduces to $f(\mathbf{Q})$ and one gets full scattering amplitudes at all the lattice points of the reciprocal lattice of $\mathbf{R}$. However, if a basis consisting of more than one atom, the unit cell structure factor has to be evaluated as certain reflections may disappear or their intensity may vary.

To illustrate this, the scattering amplitude of a FCC crystal with a cubic lattice and a base consisting of atoms in (000), (1/2,1/2,0), (0,1/2,1/2), and (1/2,0,1/2) is calculated. Here the unit cell structure factor becomes

$$f(\mathbf{Q})\sum_j e^{i\mathbf{Q}\cdot\mathbf{r}_j} = f(\mathbf{Q})(e^{i0} + e^{i\mathbf{Q}\cdot(\mathbf{a}_1/2+\mathbf{a}_2/2)} + e^{i\mathbf{Q}\cdot(\mathbf{a}_2/2+\mathbf{a}_3/2)} + e^{i\mathbf{Q}\cdot(\mathbf{a}_1/2+\mathbf{a}_3/2)}) =$$

$$f(\mathbf{Q})(1+e^{i\pi(h+k)}+e^{i\pi(k+l)}+e^{i\pi(h+l)}) = f(\mathbf{Q})\begin{cases}4 & \text{if } h,k,l \text{ are all even or odd}\\ 0 & \text{if } otherwise\end{cases}$$

Hence, only reflections with h,k, and l all even or odd will give a scattering amplitude. This is shown in Figure 4.2a, which shows which reflections will have non-vanishing scattering amplitude for an FCC crystal. It should be noted that the resulting reciprocal lattice in Figure 4.2a ends up being a BCC lattice. Conveniently, a BCC lattice will end up as an FCC lattice in reciprocal space. This makes the interpretation of the diffraction data easier for an FCC and BCC crystal.

Evaluating the scattering amplitude from a compound, such as Cu_2O, becomes a bit more complicated. Different atoms in the unit cell are taken into account in the unit cell structure factor by using the respective atoms $f_j(\mathbf{Q})$ in the sum. For Cu_2O (see Figure 3.1), the basis has an oxygen atom at (0,0,0) and (1/2,1/2,1/2) and a Cu atom at (1/4,1/4,1/4), (1/4,3/4,3/4), (3/4,3/4,1/4), and (3/4,1/4,3/4). The resulting unit cell structure factor becomes

$$\sum_j f_j(\mathbf{Q})e^{i\mathbf{Q}\cdot\mathbf{r}_j} = f_O(\mathbf{Q})(e^{i0} + e^{i\mathbf{Q}\cdot(\mathbf{a}_1/2+\mathbf{a}_2/2+\mathbf{a}_3/2)}) + f_{Cu}(\mathbf{Q})(e^{i\mathbf{Q}\cdot(\mathbf{a}_1/4+\mathbf{a}_2/4+\mathbf{a}_3/4)}$$
$$e^{i\mathbf{Q}\cdot(\mathbf{a}_1/4+3\mathbf{a}_2/4+3\mathbf{a}_3/4)} + e^{i\mathbf{Q}\cdot(3\mathbf{a}_1/4+3\mathbf{a}_2/4+\mathbf{a}_3/4)} + e^{i\mathbf{Q}\cdot(3\mathbf{a}_1/4+\mathbf{a}_2/4+3\mathbf{a}_3/4)}) =$$
$$f_O(\mathbf{Q})(1 + e^{i\pi(h+k+l)}) + f_{Cu}(\mathbf{Q})(e^{i\pi(h/2+k/2+l/2)} + e^{i\pi(h/2+3k/2+3l/2)} + e^{i\pi(3h/2+3k/2+l/2)}$$
$$+e^{i\pi(3h/2+k/2+3l/2)})$$

There will still be reflections that vanish, such as (1,0,0)

$$f_O((\mathbf{1,0,0}))(1+e^{i\pi}) + f_{Cu}((\mathbf{1,0,0}))(e^{i\pi(1/2} + e^{i\pi(1/2} + e^{i\pi(3/2)} + e^{i\pi(3/2)} =$$

$$f_O((\mathbf{1,0,0}))(1-1) + f_{Cu}((\mathbf{1,0,0}))(i+i-i-i) = 0.$$

The resulting scattering amplitudes for Cu_2O can be seen in Figure 4.2b. Certain reflections will have a higher amplitude then other reflections, as $f_{Cu} < f_O$. It should be noted that the resulting diffraction pattern of a FCC crystal (like Cu) and the compound Cu_2O have some similarities. The intense reflections will create a BCC lattice, just as the FCC crystal, due to the fact that Cu, which lies in a FCC sublattice, scatters the X-rays much stronger then O. However, these "strong" reflections of Cu_2O will not lie in the same positions in reciprocal space as Cu due to the difference in lattice constants.

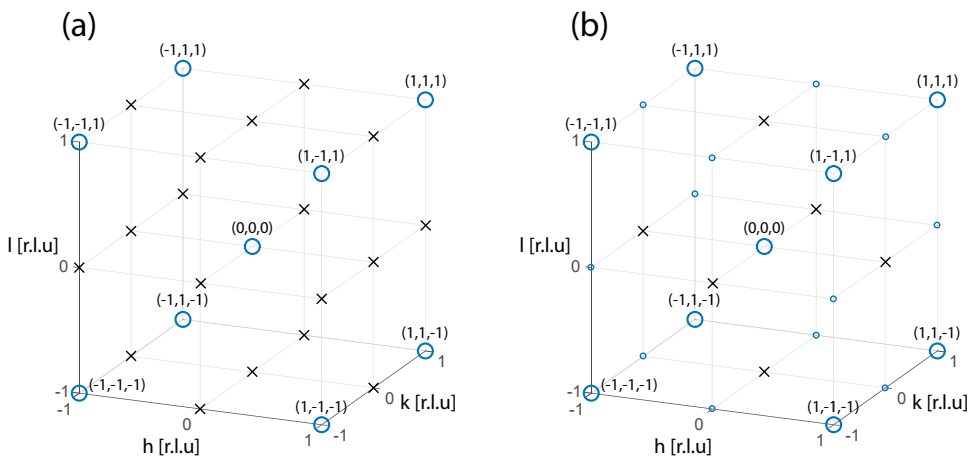

Figure 4.2: Scattering amplitude for (a) a FCC crystal and (b) a Cu_2O crystal. From the diffraction pattern it can be seen that the resulting FCC scattering amplitude becomes a BCC lattice. The blue rings show where the bragg reflections will exist and the black crosses are the reciprocal lattice points that are canceled. The size of the rings indicate the magnitude of the scattering amplitude.

The Ewald sphere

An intuitive way to visualize diffraction in reciprocal space is the Ewald sphere; see illustration in Figure 4.3. The Ewald sphere is constructed by having the

incoming k-vector, $\mathbf{k}_{in}$, pointing at a lattice point defined as the (0,0,0) point and then drawing a sphere having the radius of k_{in} around the starting point of $\mathbf{k}_{in}$. According to the Laue condition, only $\mathbf{k}_{out}$ that results in a $\mathbf{Q}$ that is equal to a reciprocal lattice vector will give constructive interference. This is fulfilled for all reciprocal lattice points that cut the Ewald sphere. The reciprocal space can then be explored by rotating the crystal, as more reciprocal lattice points will cut the Ewald sphere.

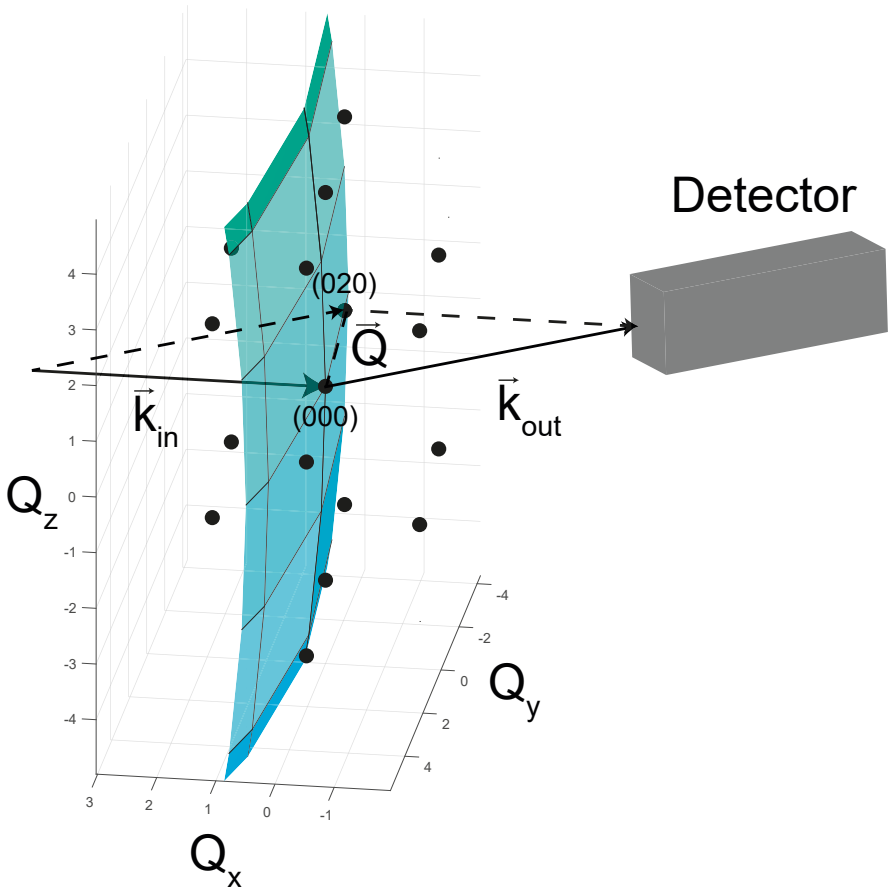

Figure 4.3: Illustration of the Ewald sphere with a sphere radius of 35.72 $Å^{-1}$, 70.5 keV, and the reciprocal lattice of Cu. The Cu lattice is rotated by 3.5° around the [001] direction, such that the (020) reciprocal lattice point cuts the Ewald sphere. The incoming ($\mathbf{k}_{in}$), outgoing ($\mathbf{k}_{out}$) k-vector, and the Q-vector ($\mathbf{Q}$) are shown in the figure. As the (020) lattice point cuts the Ewald sphere $\mathbf{k}_{out}$ will result in a Bragg reflection.

1.2 Surface X-ray Diffraction

As the processes of interest in this thesis take place on the surface and not the bulk, the method used should measure the top-most layers of atoms. This is possible with Surface X-ray diffraction, which uses a gracing incident X-ray beam close to the critical angle, to maximize surface sensitivity. Although a monolayer of atoms scatters X-rays weakly, the use of high flux synchrotron light makes it possible to get measurable diffraction from the surface.

For an infinite perfect crystal, the lattice sum will give delta functions at the reciprocal lattice points. This means that for a 3D crystal, one will get sharp diffraction spots at $\mathbf{Q}$=$\mathbf{G}$. However, if a surface is introduced, the periodicity will be broken perpendicular to the surface, giving streaks of scattering intensity in this direction, see Figure 4.4. This is called Crystal Truncation Rods (CTRs).

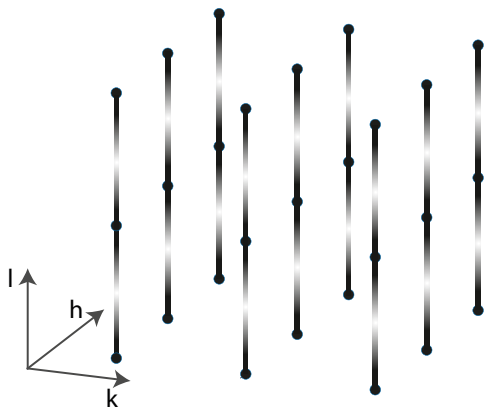

Figure 4.4: Illustration of CTRs connecting the Bragg reflections. The dots show the Bragg reflections of a simple cubic crystal structure, where the surface lies in the z-direction (parallel to l).

To better understand how CTRs appear, we can consider a 3D crystal with a surface. To get the scattering amplitude in the direction perpendicular to the surface, we only need to consider the lattice sum in this direction, $\mathbf{a}_3$. The lattice sum for the two other directions, parallel to the surface, will create delta functions at the reciprocal lattice points. If A($\mathbf{Q}$) is the scattering amplitude for one layer of atoms, the scattering amplitude for an infinite stack of such layers becomes[1]

[1] We have that $\sum_{t=0}^{\infty} p^t = \frac{1}{1-p}$ if $\mid p \mid < 1$

$$F^{CTR} = A(\mathbf{Q}) \sum_{n=0}^{\infty} e^{iQ_z a_3 n} = \frac{A(\mathbf{Q})}{1 - e^{iQ_z a_3}}$$

The intensity of the CTRs then become

$$I^{CTR} = \mid F^{CTR} \mid^2 = \frac{\mid A(\mathbf{Q}) \mid^2}{(1 - e^{iQ_z a_3})(1 - e^{-iQ_z a_3})}$$

If we instead write Q_z as $2\pi l/a_3$, where l is a continues variable, the above equation becomes

$$I^{CTR} = \frac{\mid A(\mathbf{Q}) \mid^2}{4 \sin^2(\pi l)} \tag{4.3}$$

Hence, if we introduce a surface there will be a scattering intensity outside of the reciprocal lattice points. This can be seen in Figure 4.6 where the black line is Equation 4.3 plotted, with $\mid A(\mathbf{Q}) \mid = 1$. It should be noted that the above equation is not defined at the Bragg points where the intensity diverges.

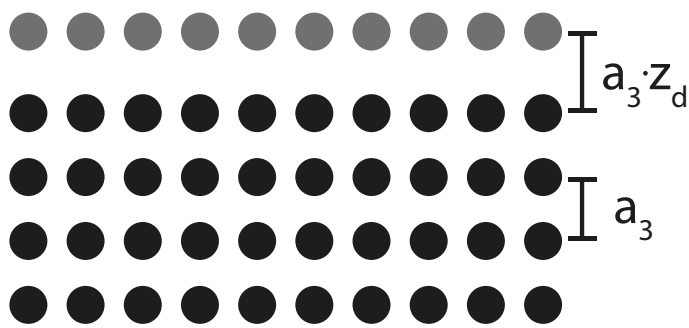

Figure 4.5: Periodic arrangement of atomic layers with a spacing of a_3. The top most layer is displaced by a factor of z_d.

If we introduce an additional layer of atoms that are displaced by z_d relative from the lattice spacing a_3, see Figure 4.5. The above sum would then have one extra term of $A(\mathbf{Q})e^{iQ_z(a_3+z_d a_3)n}$ at n=-1. This means that the sum becomes

$$F^{CTR} = \frac{A(\mathbf{Q})}{1 - e^{iQ_z a_3}} + A(\mathbf{Q}) e^{-iQ_z(a_3+z_d a_3)} = \frac{A(\mathbf{Q})}{1 - e^{i2\pi l}} + A(\mathbf{Q}) e^{-i2\pi l(1+z_d)} \tag{4.4}$$

The effect of the n=-1 atomic layer can be seen in Figure 4.6, where three different values of Z_d is compared with the surface with bulk periodicity. It can be clearly seen that the intensity variation of the CTR changes with a surface that has different spacing than the bulk. This can be used to calculate the surface structure.

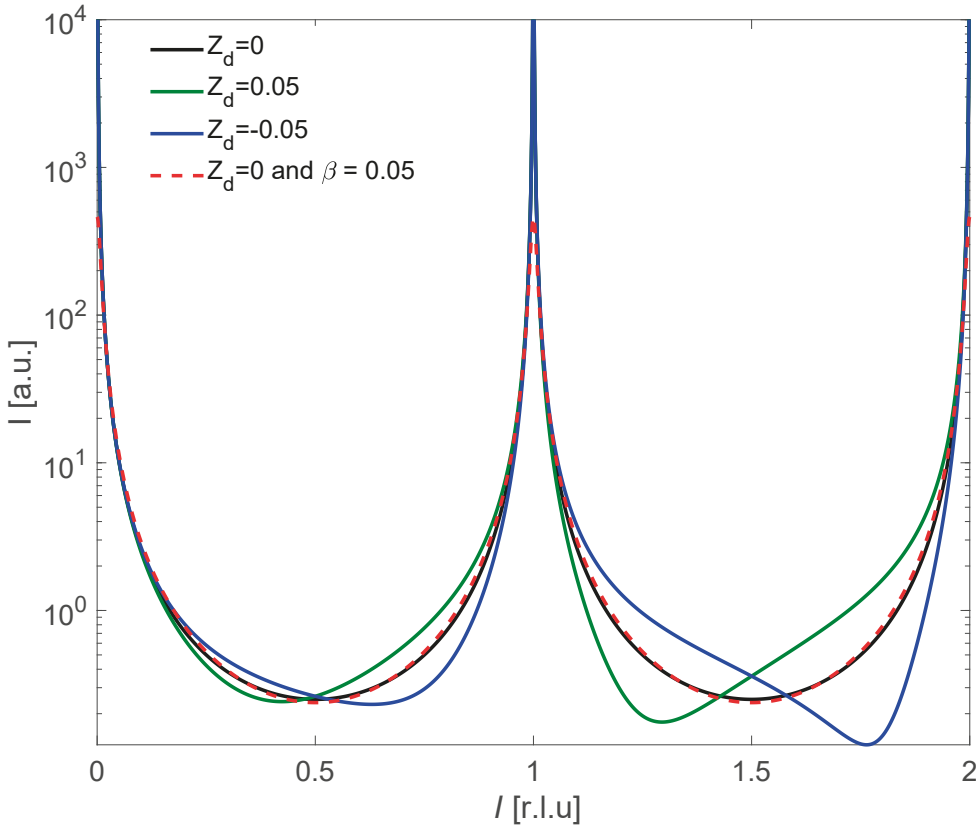

Figure 4.6: Calculation of CTRs from equation 4.4 for various values of Z_d, where Z_d=0 shows the surface with bulk periodicity, and with absorption. The intensity is calculated, which is $\mid F^{CTR} \mid^2$. A(**Q**)=1 is used for simplicity. Close to the bragg peak there is no difference between the different surfaces as the intensity diverges, expect for the case with absorption where the bragg peak have finite intensity. The effect of the displacement of the surface from the bulk periodicity increases with increasing *l*.

It should be noted that the description of the CTR above only would be valid if there is a dampening effect for the scattering amplitude with increasing depth. The scattering amplitude for an infinite periodic stack of atoms, with period a_3, would yield a delta function with the spacing of $2\pi/a_3$. However, a stack of atoms from $(0, \infty)$, as described above, is still an infinite stack of atoms and should yield delta functions with the spacing of $2\pi/a_3$. This, however, does not seem to be the case as we do not see delta functions but instead a continuous

varying scattering amplitude. The reason for this is that there is an inexplicit dampening effect in the description of F^{CTR}. The sum, which is a Fourier transform of the step function, is calculated using the Fourier transform of an antisymmetric decaying exponential function e^{-ax} with a $\rightarrow 0$. Thus there is a dampening effect embedded in the description.

Dampening of the X-rays with increasing depth is realistic as the X-ray intensity decreases with depth due to scattering and absorption. Hence, a more accurate description of the scattering amplitude would be to add an explicit dampening effect, in terms of absorption of the X-rays. This is done by adding a term of $e^{-\beta}$ to the sum. Here β is the absorption parameter per layer $a_3\mu/sin(\theta)$, where μ is the absorption length and θ the incoming angle. This description assumes that the incoming angle is equal to the outgoing angle. The result would give finite intensity at integer values of l, or at the Bragg peaks, which is more realistic, see Figure 4.6.

1.3 Instrumentation

This thesis has conducted the SXRD experiments at beamline P21 at Petra III and beamline I07 at Diamond. An illustration of the experiments is shown in Figure 4.7. The sample sits on a diffractometer where the sample can be aligned. First, the sample is aligned such that the incoming beam is parallel to the sample surface. The incident angle, α, is set close to the critical angle, which for hard X-rays[2] is small, 0.05° used in Paper IV. A large 2D detector is positioned in front of the chamber and is used to measure the scattered beam. Due to the high flux of the synchrotron, tungsten blocks are placed at spots on the detector where the Bragg reflections appear to prevent any damage to the detector.

Commonly, an orientation matrix is needed and is created by finding the ω and detector positions for two Bragg reflections, which are used as reference. The orientation matrix is then used to orient in reciprocal space and find specific reflections. However, with the large 2D detector, an orientation matrix is not needed, simplifying the experiment.

After aligning, the experiments in this thesis are straightforward; one heats the sample and doses gases to desired values, ω is rotated for a set range and steps, where a detector image is taken for each step. The detector image measures a projection of the Ewald sphere where, as described in section 2.1, the reflections that coincide with the Ewald sphere show up in the detector. During the ω

[2]Hard X-rays are usually referred to X-rays with energy larger then 5 keV

rotation, the reciprocal space will also rotate, leading to new reflections showing up in the detector. Hence, the reciprocal space can be explored by rotating ω.

The setup at Diamond is a larger UHV chamber with a capacity of LEED as well. The heating is done by electron bombardment, which limits the pressure range that can be used. However, the setup used at Petra III is a more compact UHV chamber with a boralectric heater. The chamber also has the capacity to dose gases at elevated pressures. Both setups have the capacity to clean the surface by Ar sputtering.

A general issue with the setups is beryllium scattering, with appears as bright rings on the detector image. This comes from the scattering of the windows used on the vacuum chamber; beryllium is used to minimize the beam attenuation. The beryllium scattering from the outgoing beam can easily be blocked by placing a lead peace in front of the exciting window. However, the beryllium scattering from the incoming beam is not as easily blocked. It is possible to block some of the scatterings with tungsten masks but this comes at a price of also blocking some the scatted beam from the sample.

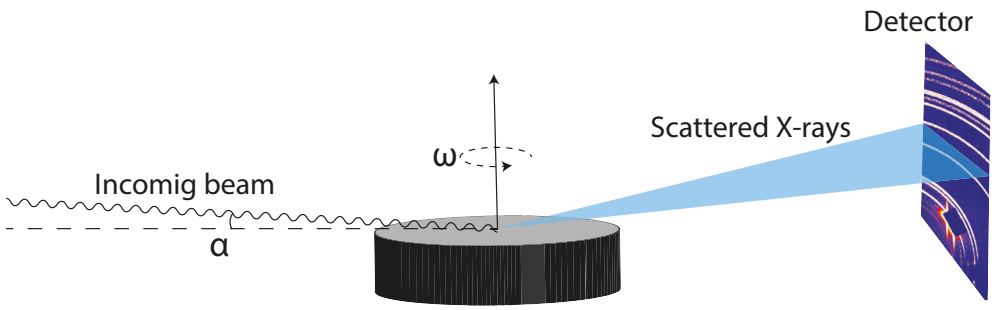

Figure 4.7: Illustration of SXRD experiment, as conducted in the thesis.

1.4 Data Analysis

As mentioned above, the data images are projections of the Ewald Sphere. As the radius of the Ewald sphere is growing with the photon energy, there is an advantage of using hard X-rays as the curvature of the Ewald sphere is

flatter. This means that the detector image becomes closer to a plane in the reciprocal space. Nevertheless, any accurate analysis needs to transform the detector images to reciprocal space.

To transform the detector images to reciprocal space, the Q-vector for each pixel has to be calculated. The Q-vector at pixel P=(x,y) can be calculated from

$$\mathbf{Q} = \mathbf{k}_{in} - \mathbf{k}_{out} = \mid \mathbf{k} \mid [(0,0,1) - \frac{(\Delta P \times (x_{DB} - x), \Delta P \times (y_{DB} - y), z_d)}{\sqrt{(\Delta P \times (x_{DB} - x))^2 + (\Delta P \times (y_{DB} - y))^2 + z_d^2}}]$$

where ΔP is the pixel size and z_d the distance from the sample to the detector. The $(x_{DB} - x)$ and $(y_{DB} - y)$ terms are the distance, in pixels, in the y and x-direction from P to the direct beam, see figure 4.8.

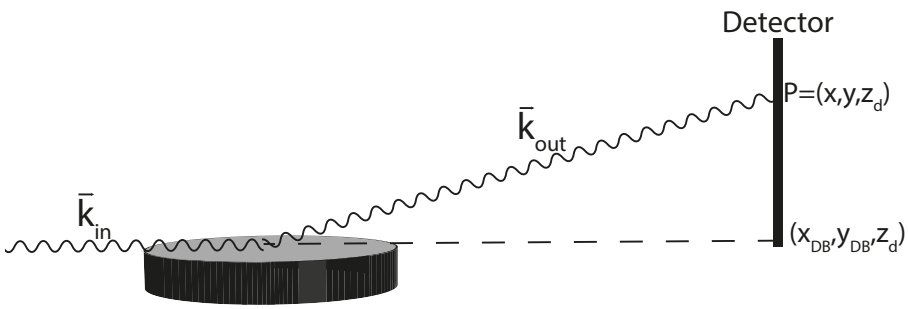

Figure 4.8

Figure 4.9 shows an example of a detector image transformed into reciprocal space. Figure 4.9a is created by subtraction of a dark image from the raw detector image and selecting the highest intensity of each pixel in the detector images for the ω rotation around the (101) reflection. The resulting image from using the equation above can be seen in (b), and the effect of the curvature of the Ewald sphere can be seen in the middle part.

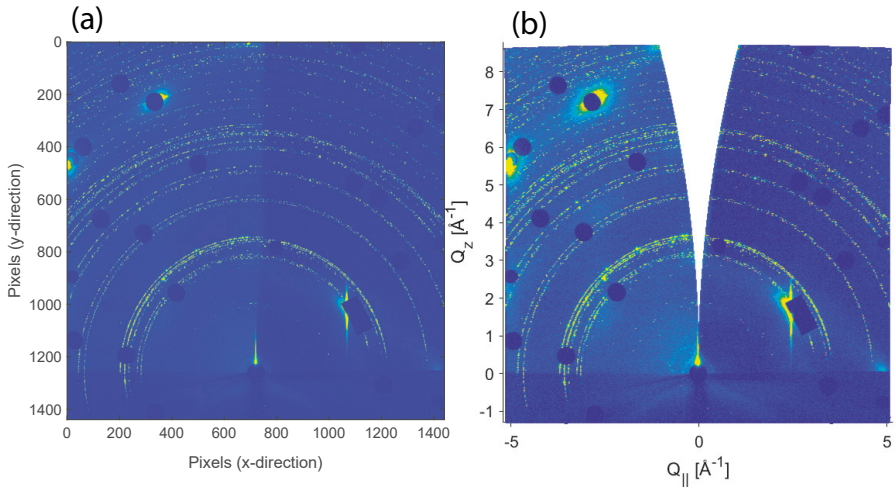

Figure 4.9: (a) show the detector image, with the dark image subtracted, from a clean Cu(911) surface. The detector image is created by summing the detector images for the ω rotation around the (101) Bragg reflection. (b) shows the detector image in Q-space. The y-direction is parallel to the normal of the surface (z-direction of the sample) and the x-direction is in the surface plane. The $Q_{||}$ direction lies in the (h,k) plane with the exact direction not obvious, however as the Ewald sphere crosses the (101) reflection it should be the h-direction. A CTR can be seen at the (101) Bragg reflection. The darker spots on the image are tungsten blocks that protect the detector from the high intensity Bragg reflections. The bright rings are scattering from the beryllium window.

2 Photoelectron Spectroscopy

The phenomenon of the photoelectric effect was first discovered by Hertz in 1887, who observed that ultra-violet light caused electrons to emit from different materials. However, it was first later that the phenomenon was systematically studied by varying the wavelength of the impinging light and measuring the maximum kinetic energy of the electrons, which showed that the kinetic energy was connected to the wavelength of the light and the work function [33]. A. Einstein later described the photoelectric effect with the introduction of the quantum nature of light, for which he was rewarded the Nobel Prize in 1921 [34]. The fundamental equation that governs photoemission is

$$E_{kin} = h\upsilon - E_{Bin} - \Phi,$$

where E_{kin} is the measured kinetic energy of the electrons, $h\upsilon$ is the energy of the photons, E_{Bin} is the binding energy of the electrons in the material, relative to the fermi level, and Φ is the work function of the material. The overall principle of photoemission is illustrated in Figure 4.10a, where an electron absorbs a

photon, which has high enough energy for the electron to escape to the vacuum level. The electron's kinetic energy will then be the difference between the energy of the photon and the electron's binding energy plus the work function. As the binding energy of electrons is different for different chemical elements, the photoelectron can identify the element of origin. This is especially clear for core-levels where the difference in binding energy is significant; for example, the difference between the 1s electrons in O and C is around 250 eV.

K. Siegbahn further developed the field of photoemission by discovering that the binding energies of the core levels in atoms are sensitive to the chemical surroundings of the photoemitting atom, which lead to the use of Photoelectron Spectroscopy (PES) as a tool for chemical analysis. K. Siegbahn was rewarded the Nobel Prize in 1981 for his work on developing Electron Spectroscopy for Chemical Analysis (ESCA) [35].

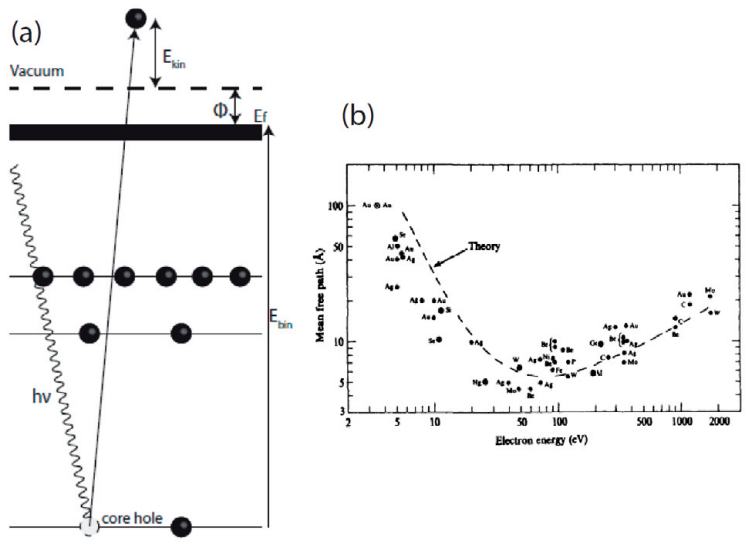

Figure 4.10: (a) Schematic illustration of the principal of XPS. (b) The universal curve of the electron mean free path as a function of the kinetic energy of the electrons. (b) is from ref. [36]

The easiest way to describe PES is by the simplification of the three-step model, which separates the process into three distinct, independent steps; (1) a photon is absorbed locally, which excites an electron resulting in photoionization, (2) the electron travel through the sample to the surface, and (3) finally the electron escape to the vacuum level where it is detected. The intensities of the photoemitted electrons versus the kinetic energy are measured and can be plotted. To obtain the spectrum of the electrons levels, the binding energy of the

electrons is used instead, which can be calculated by rearranging the above equation to,

$$E_{Bin} = h\upsilon - E_{kin} - \Phi.$$

An important property of PES is the surface sensitivity of the technique, as the penetration depth of the photoelectrons is shallow. This can be seen in 4.10b, which shows the inelastic mean free path of electrons in the kinetic energy range typical for PES. As the mean free path of the electrons is of the order of Å, a large part of the signal will originate from the surface, making it a suitable technique to study surface chemistry and heterogeneous catalysis. PES refers to a set of experimental techniques, e.g., ultraviolet photoelectron spectroscopy studying the valence electrons and angular-resolved photoemission spectroscopy studying the band structures. However, only core-levels are used in this thesis, which is usably referred to as XPS or core-level spectroscopy.

The advantage of studying the core-levels is that the binding energy difference between the core-levels of different materials is large compared to the valence levels, thus making it easier to distinguish elements from each other. Also, the binding energies of the core-levels change with the chemical environment around the photoemitting atom, making it possible to distinguish different chemical states. This "chemical shift" can be used as a fingerprint of various surface structures and adsorbed species. This is illustrated in Figure 4.11, where the chemical shift in the O 1s level for O/Cu(100) is shown. The shift between the MR structure and the p(2×2) is observed to be around 0.5 eV. The calculated shift between the two structures is reported to be 0.7 eV in Paper I.

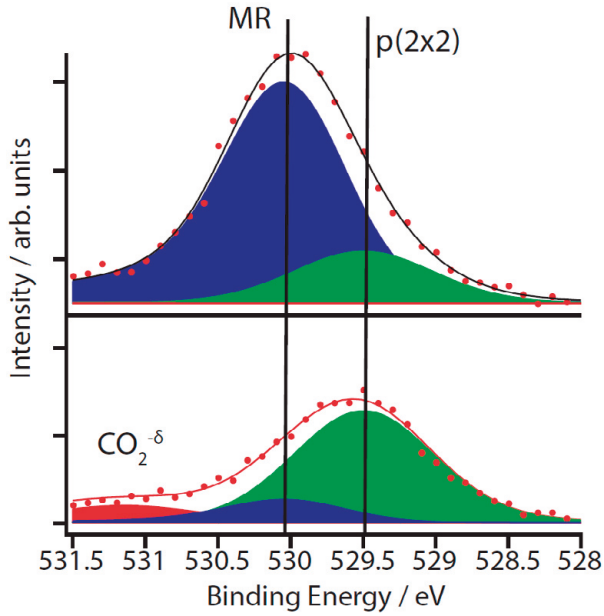

Figure 4.11: O 1*s* spectra at 0.4 mbar and 100 °C. The green, blue, and red peaks are the p(2×2), MR, and chemisorbed CO_2, respectively.

2.1 Ambient Pressure X-ray Photoelectron Spectroscopy

Typically, XPS is performed under UHV conditions, as the electrons will otherwise scatter from the gas molecules on their way to the analyzer. However, as the interaction of CO2 and Cu is weak, the experiments have to be performed at higher pressures. Operating XPS under higher pressures can be achieved by using a differentially pumped aperture that is placed close to the sample. This concept was first developed by Siegbahn et al. in the late 1960s [37]. Later on, APXPS was developed with the use of differentially pumped electrostatic lens systems, enhancing the transmission and making it possible to perform XPS measurements in the mbar range [38].

A schematic illustration of the principle of APXPS is shown in Figure 4.12. The sample is placed in close proximity to an aperture with a narrow opening. The electrons will travel along several differentially pumped stages to reduce the pressure from mbar, at the sample, to UHV in the hemispherical analyzer. Electrostatic lenses will focus the electrons into the apertures between the different stages leading to an enhancement of the transmission.

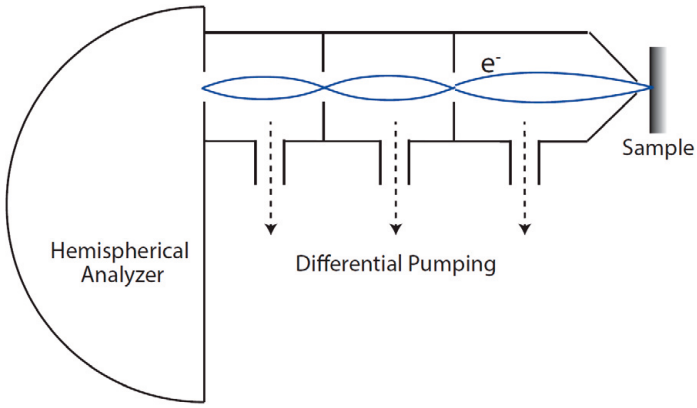

Figure 4.12: Schematic drawing of the AP-XPS setup.

APXPS has the advantage of being able to operate at pressures from UHV to mbar, enabling experimental conditions more realistic for catalysis compared to traditional XPS. However, many catalytical chemical reactions are operating far above the mbar range. Additionally, the signal-to-noise ratio and energy resolution are typically reduced in APXPS compared to UHV XPS.

2.2 Data analysis

The core-levels do not show up as infinitely narrows lines in the XPS spectrum but are broadened with specific line shapes, which have its origin in both internal properties of the system and the experimental setup. There are several different contributions to the line broadening.

The first contribution comes from the lifetime of the core hole created in the photoemission process due to the Heissenberg uncertainty principal, i.e., $\Delta E \times t \geq \hbar/2$. This broadening is described by a Lorentzian lineshape,

$$L(E) = \frac{1}{[1 + (\frac{E_0 - E}{\gamma})^2]},$$

where E_0 is the peak position and 2γ the FWHM.

When leaving the sample, the photoelectrons can interact with electrons in the valence band creating electron-hole pairs in the valence band, making the photoelectrons lose kinetic energy in the process. This interaction will manifest itself as an asymmetry in the line shape towards higher binding energies. Thus,

to adequately describe the line shape of the peaks, a Doniach-Sunjic profile is used, instead of a Lorentzian, which has a parameter describing the line shape asymmetry,

$$f(E) = \frac{\Gamma(1-\alpha)}{(\gamma^2 + E^2)^{(1-\alpha)/2}} \cos(\frac{\pi\alpha}{2} + (1-\alpha)\arctan(E/\gamma)),$$

where Γ is the Gamma function and α is the asymmetry parameter.

The other contributions to the broadening of the lines come from the energy resolution of the analyzer, atomic vibrations, energy distribution of the X-ray beam, etc. These contributions are modeled with a Gaussian function, which then is convoluted with the Doniach-Sunjic lineshape to form the final line shape.

The photoemission spectra are analyzed by fitting a set of peaks with line shapes as described above. Five different parameters are fitted for each peak; binding energy, FWHM of Gaussian, FWHM of Lorentzian, asymmetry, and peak height. A background originating from in-elastic scattered electrons is also included in the fitting procedure.

3 Scanning Tunneling Microscopy

Scanning Tunneling Microscopy (STM) is an imaging technique, which as its name suggests, relies on the quantum tunneling effect to achieve a resolution down to the sub-Ångstrom regime, enabling structural characterization of the surface on the atomic level. The STM was invented in 1981 by B. Binnig and H. Rohrer, for which they received the 1986 Nobel Prize in Physics [39], and since its discovery, STM has been widely used as a tool for surface characterization in surface science.

Figure 4.13a shows the working principle of the STM, where a sharp metal tip is placed in close vicinity to the surface, and a voltage is applied between the tip and the surface, which will create a measurable tunneling current. To obtain an image of the surface, the tip is scanned across the surface, using piezo-scanners, as the current is measured, resulting in a picture of the density of states at the surface [40]. What is described above is called constant height mode, as the height of the tip is kept constant throughout the measurement. However, a more widely used method is the constant current mode which uses a feedback loop to adjust the height of the tip above the surface such that the measured current is constant.

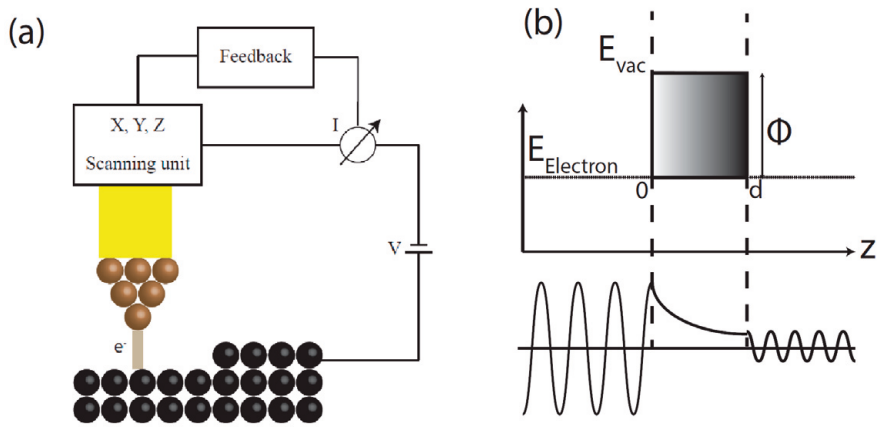

Figure 4.13: (a) schematic illustration of the STM working principal. (b) schematic illustration of the tunneling concept. The gray area is the classically forbidden region while the left is the sample and the right the tip. Below the energy diagram the real part of the wave-function is seen. The wave-function of the electron decays exponentially outside the surface.

As mentioned above, the STM utilizes the quantum tunneling effect to achieve atomic resolution. This can be understood by considering the simplest case, as seen in Figure 4.13b, with a 1D potential V(z) with constant value V_0 in-between Z=0 and Z=d. The electrons outside the barrier are assumed to be free and have an energy $E_e < V_0$, and thus it would be impossible for the electrons to pass the barrier if only classical mechanics were considered. However, taking quantum mechanics into account, the electrons are described by the wave function, $\Psi(t, z)$, which solves the Schrödinger equation. By solving the time-independent Schrödinger equation, it is found that the wave-function within the barrier will be exponentially decaying as

$$\psi = \psi(0)e^{-\kappa z},$$

where $\kappa = \sqrt{\frac{2m}{\hbar}(V_0 - E_e)}$ and m is the mass of the electrons. The probability of an electron to be found on the other side of the barrier is,

$$\mid \psi(d) \mid^2 \propto e^{-2\kappa z}.$$

Thus, quantum mechanics predicts that there is a non-zero probability of electrons to tunnel through the barrier. As the current is proportional to the probability of electrons tunneling to the other side of the barrier, the current will also decay exponentially with the distance between the tip and the surface. Using

a barrier height of 4.5 eV, typical of a work-function, and the mass of a free electron, the tunneling probability, and thus the current, will drop by a factor of 10 for an increase in distance of 1 Å. This makes it possible to measure small changes in the distance between the tip and the surface and explains the good vertical resolution of STM.

Figure 4.14 shows an STM image of the MR structure on Cu(100), see Figure 3.5c, with the corresponding unit cell. The figure illustrates the ability of STM to resolve structures on the atomic level. It should be noted that the image contrast of the MR structure on Cu(100) depends drastically on the tip, metal or oxygen terminated, and the bias voltage [41].

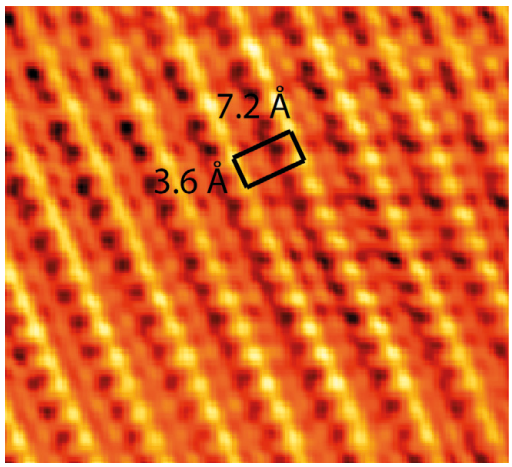

Figure 4.14: STM image of the MR structure illustrating the atomic resolution of STM. The black rectangle show the unit cell of the MR. The surface was prepared by dosing 1200 L of O_2 at 100 °C. The image has been improved by using fourier transform filtering to reduce the noise. The tunneling conditions are 0.8 V and 200 pA.

4 Low Energy Electron Diffraction

Low Energy Electron Diffraction (LEED), is a well-established technique in surface science for qualitative surface structure characterization. Just as X-ray diffraction, LEED utilizes the wave nature of electrons, giving diffraction effects, to achieve a picture of the reciprocal surface lattice. In LEED, a monochromatic electron beam impinges on the surface, and the backscattered electrons will have intensity maxima in specific directions. The electrons are detected by a fluorescent screen, which will create a "LEED image" of the surface. It can be shown that the electrons will only interfere constructively if the change of momentum, parallel to the surface, is equal a reciprocal surface lattice vector

[42], i.e.

$$\Delta \mathbf{k}_{\parallel} = \mathbf{G}$$

Thus, the diffraction pattern seen on the fluorescent screen will correspond to the reciprocal surface lattice.

LEED uses electrons with energy in the range of 20-200 eV, which means that, just as in the case of XPS, the signal will mostly originate from the topmost layers of the sample, thus making LEED a surface sensitive method. This also implies that the LEED image will contain diffraction spots from the surface structure as well as the substrate, which usually makes it straightforward to determine the Wood's notation of the surface.

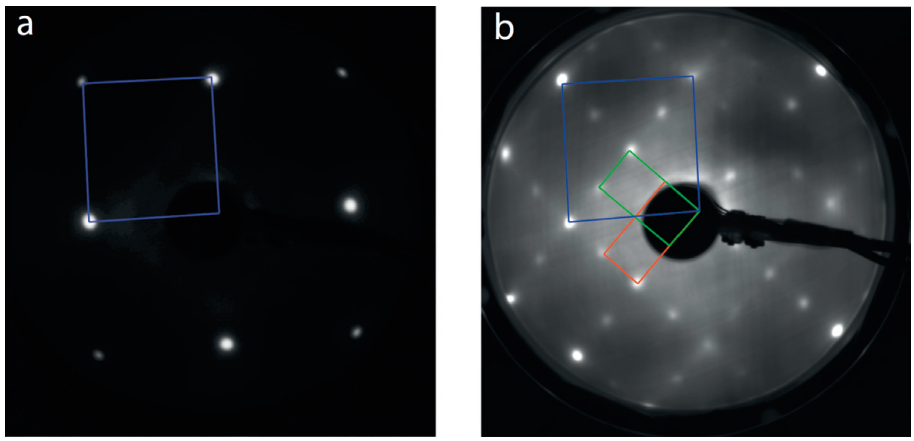

Figure 4.15: (a) LEED image of the pristine Cu(100). (b) LEED image of the MR structure on Cu(100). Blue square show the unit cell of the reciprocal lattice of Cu(100). Green and red rectangle show the unit cell of the two domains of the MR structure on Cu(100).

LEED has been used throughout this the thesis as a tool for a qualitative characterization of the surface before and after sample preparation. Examples are shown in Figure 4.15, showing two LEED images from a pristine Cu(100) surface and a Cu(100) surface prepared with the missing row structure, respectively.

5 Density Functional Theory

Density Functional Theory (DFT) is a powerful computational method for calculating the electron structure, which can be used to solve various problems

in surface science. I have not performed any of the DFT calculations for this thesis; however, as it has been used as a compliment to the experiments, a brief description of DFT is provided. DFT has been used in paper I as a way to calculate the energies of the surface structures and the corresponding CLS of O 1s. In paper II, DFT has been used to propose a mechanism for CO_2 dissociation on Cu(100), and the corresponding energy barriers.

The electronic wave-function, $\Phi(\mathbf{r}_1,\mathbf{r}_3,\mathbf{r}_3,...,\mathbf{r}_N)$, of a system with N electrons gives the electronic structure of the system. This wave-function is determined by solving the Schrödinger equation

$$H\Phi = (T + V + U)\Phi = E\Phi,$$

where the Hamiltonian (H) contains the kinetic energy (T), the potential energy from the electrostatic field of the nuclei (V), and the electron-electron interaction energy (U). Due to the many-body nature of the problem, it is impossible to solve the above equation with an analytical form, except for the most simple cases. Therefore, a numerical calculation has to be done; however, with 3N parameters, it becomes computational unfeasible and approximations have to be made [24].

DFT is based on two theorems by Hohenberg and Kohn, who showed that in a system with interacting electrons in an external potential, the ground state electron density $n(\mathbf{r})$ can uniquely determine the potential. The ground state density, thus, determines all the ground state properties of the system [43]. The electron density that minimizes the energy is the correct ground state. Kohn and Sham showed that the many-body system can be replaced with a set of self-consistent single-electron equations that will give the same electron density as the many-body system [44]. This is the so-called Kohn-Sham equations

$$(T + V_{eff})\phi_i(\mathbf{r}) = (T + v_{ext}(\mathbf{r}) + v_H(\mathbf{r}) + v_{xc}(\mathbf{r}))\phi_i(\mathbf{r}) = \epsilon_i\phi_i(\mathbf{r}),$$

where V_{eff} is the effective external potential from the nuclei (v_{ext}), the Hartree energy (v_H), and the exchange-correlation potential (v_{xc}). All terms in the above equation are known, except v_{xc} which contains all quantum mechanical effects, such as the antisymmetry of the electronic wave function (exchange) and the electron-electron correlation. v_{xc} is the functional derivative of the exchange-correlation functional $E_{xc}[n]$, thus if $E_{xc}[n]$ is known v_{xc} can be obtained. However, in DFT, the approximation is done by using different functionals as an approximation of $E_{xc}[n]$.

Ab initio thermodynamics

Several experimental techniques can investigate the surface structures. However, calculations using *ab initio*[3] thermodynamics is a powerful method complementing the experiments [45]. The principle of the *ab initio* thermodynamics is to calculate the surface free energy, γ, as a function of the chemical potential, $\mu(T, p)$, of the species of interest. As the topic of this thesis is the oxidation of the surface, the oxygen chemical potential is of interest. Thus, *ab initio* thermodynamics calculations are used in this thesis to calculate the surface free energy as a function of the oxygen chemical potential to evaluate the stability of the different structures.

In paper I, *ab initio* thermodynamics calculations were used to examine the oxidation of Cu(100) by examining the relative stability of structures considered in the paper, as well as experimentally investigate the evolution of the surface with *in-situ* XPS. The surface free energy is calculated by the following equation,

$$\gamma(T, p) = \frac{1}{A}[E_{\mathrm{O/Cu}} - E_{\mathrm{Cu}} - N_{\mathrm{Cu}}\mu_{\mathrm{Cu}} - N_{\mathrm{O}}\mu_{\mathrm{O}}(T, p)],$$

where $E_{\mathrm{O/Cu}}$ is the total energy of the oxygen covered surface and E_{Cu} is the total energy of the pristine surface, which are calculated from DFT. $\mu_{\mathrm{O}}(T, p)$ and N_{O} are the oxygen chemical potential and number of oxygen atoms in the surface cell, respectively. $N_{\mathrm{Cu}}\mu_{\mathrm{Cu}}$ accounts for the cost of bringing N_{Cu} Cu atoms from and to the bulk. Using the above expression, the surface free energy of a surface structure as a function of the oxygen chemical potential can be evaluated.

[3] ab initio calculations are referred to calculations that are from first principles, i.e., it only uses the established laws of nature and does not add any assumptions.

Chapter 5

Summary of Papers

In Paper I and II the low-index Cu(100) was studied with the conclusion that the steps dominates the dissociative adsorption of CO_2, and not the (100) terraces. Paper III-V acts as a follow up on paper I and II, where the goal is to validate the model presented in paper II. This is done by studying the vicinal Cu(911) surface, which consist of (111) steps every ∼11.5 Å. Although it was confirmed that the steps facilitate CO_2 adsorption, the process seems to be more complicated than the model presented in paper II.

Paper I: Initial Oxidation of Cu(100) studied by X-ray photo-electron spectroscopy and density functional theory calculations

In this paper, the initial oxidation of Cu(100) by CO_2 was measured with AP-XPS. It was found that the adsorbed oxygen, from the CO_2 dissociation, initially has a peak at 529.5 eV. However, as the oxygen coverage increases, a second peak at 530 eV appears and gradually becomes the dominating peak.

The surface stability, with respect to oxygen coverage, was calculated for seven different oxygen structures with an oxygen coverage in the range of 0.124-0.50 ML. It was found that the initial oxidation of Cu(100) proceeds from a formation of a p(2×2) structure with an oxygen coverage of 0.25 ML, to the reconstructed MR structure with an oxygen coverage of 0.50 ML.

The core-level binding energy shifts of O 1s from the five most stable structures

found in the surface stability calculations, were calculated and compared to the experimental results of ∼0.5 eV. It was found that the calculated binding energy difference in the O 1s binding energy between the p(2×2) and the MR is 0.7 eV, which is in reasonable agreement with the experimental result. The shift in binding energy can be coupled to a change in coordination of the O atoms from 4 to 3 Cu atoms.

Paper II: Steps control the dissociation of CO_2 on Cu(100)

In this paper, the oxygen coverage increase from the CO_2 dissociation was studied in detail for an increased understanding of the mechanism involved in the dissociation reaction. It was found that at 100 °C in 0.4 mbar CO_2 the oxygen coverage curve has a slope change at ∼0.25 ML and saturates at ∼0.5 ML. It was also found that the oxygen coverage curve is linear in-between 0-0.25 ML and 0.25-0.45 ML. The linearity of the oxygen coverage curve suggests that, with each of the linear regimes, the CO_2 dissociation does not depend on the oxygen coverage.

DFT calculations were done to explain the experimental observations, and it was found that on the clean Cu(100) terrace, the energy barriers for CO_2 adsorption and dissociation are 0.55 and 0.83 eV, respectively. Any preadsorbed oxygen will negatively affect the stability of the adsorption of CO_2 on the terrace, and at 0.25 ML it is impossible to dissociatively adsorb CO_2. Thus, only taking the (100) terraces into account, we cannot explain the linear uptake or the oxygen coverage increase after 0.25 ML.

To explain the linear oxygen coverage increase and the oxygen coverage increase after 0.25 ML, DFT calculations were done for a stepped Cu(611) surface. The dissociation over a step has a dissociation barrier that is 0.26 eV lower compared to the terrace. After the dissociation, the CO molecule will sit in a bridge site on the upper terrace, and the oxygen atom will sit at the three-fold hcp site at the step. However, the overall energy of the configuration will be lowered if the oxygen diffuses away from the step to a four-fold hollow site on the lower terrace. This will separate the products, lowering the probability for recombination to CO_2, but also leaving the active sites available for further reaction.

Both Paper I and II illustrates the effectiveness of combining experimental work with theoretical modeling to understand processes relevant for industrial applications.

Paper III: Oxygen induced faceting of Cu(911)

As a continuation of paper I and II, the vicinal Cu(911) surface is investigated. In this paper, the initial oxidation of Cu(911) by O_2 was measured with *in-situ* SXRD to better understand which structures could be present under CO_2 reduction reactions. It was found that the surface completely facets into (410), (401), and (100). These facets are stable in the parameter range of T=RT-400 °C and p=10^{-10}-10^{-5} mbar O_2. The (410) and (401) facets are present on the surface until Cu_2O starts to grow on the surface at p>10^{-5} mbar O_2.

The (410) and (401) facets have (110) steps, and not (111) steps. Hence, the result show that the closed packed (111) steps will transform to the more open (110) steps, in the presence of oxygen on the surface. The more open (110) steps should be present for the CO_2 dissociative adsorption reaction.

Paper IV: Oxide growth on Cu(911)

In this paper, the oxide formation on Cu(911) was investigated by *in-situ* SXRD, with the same motivation as Paper III. It was found that when the oxide starts to grow on the surface, the (410) and (401) facets disappear. Instead, the surface is reformed to (911), (311), and (100). A well-ordered oxide is found to grow on the (311) facets with the orientation with respect to the Cu substrate of Cu_2O(110) || Cu(311). There is most likely an oxide on the Cu(100) and Cu(911) facets as well; however the orientation is not clear from the data.

The fit between the Cu(311) and Cu_2O lattice is almost perfect. For Cu(311) and Cu_2O(110) the distance between the Cu rows are 4.23 Å and 4.27 Å, respectively. However, for Cu(911) the distance is 11.6 Å. This explains why an ordered oxide is seen on the (311) facets and not (911). The surface of the Cu_2O(110) || Cu(311) is most likely (110), but the shape of the oxide is not known and there might be other facets that are exposed on the surface.

Paper V: CO_2 dissociation on Cu(911)

In this paper, the interaction of CO_2 and Cu(911) is investigated with *in-situ* AP-XPS. It was found that initially there is a build up of CO_2 species on the surface. As atomic oxygen appears on the surface, from the dissociation of CO_2, the adsorbed CO_2 is decreasing. This initial behaviour is in line with the

findings in paper II as the adsorbed oxygen is expected to block the adsorption of CO_2. However, as the coverage of the adsorbed oxygen starts to saturate the adsorption of CO_2 starts to grow again, with a slightly shifted O $1s$ binding energy. This is most likely due to the transformation of the (111) steps and into the more open (110) steps. According to the result in paper II, the oxygen covered (100) terraces should not be able to adsorb CO_2. But, the (110) steps seems to be able to adsorb CO_2 even in the presence of oxygen. Furthermore, the dissociation rate increases when a small amount of oxygen is introduced on the surface, which is explained with that the (110) steps are more active then the (111) steps.

The result show that the adsorption of CO_2 is facilitated by the presence of steps. However, the dissociation rate does not seem to be faster on Cu(911) compared to Cu(100). It is speculated that the reason is the smaller terraces on Cu(911), where the recombination of O and CO plays a more prominent role.

Chapter 6

Concluding remarks and Outlook

Paper I and II show how experimental observations and DFT calculations can be used to describe processes in surface reactions. Paper I gave us a better understanding of the initial oxidation of Cu(100), as well an understanding of the CLS. The results from paper II lead to the development of a model in which the steps and oxygen diffusion plays an important role. Paper III and IV increased our understanding of the oxidation of the vicinal surface Cu(911). The results from paper V lead to the conclusion that CO_2 can adsorb on the oxygen covered surface with the presence of (110) steps.

However, there are aspects of the thesis that are still not clear. For one, DFT calculations are needed to model the adsorption of CO_2 on O/Cu(410) to better understand the nature of the adsorbed CO_2. Experiments combining both AP-XPS and PM-IRRAS to get a more detailed picture of the adsorption of CO_2 on the stepped surfaces. Additionally, the experiments on dissociative adsorption of CO_2 on Cu(911) presented in Paper V should be redone before publication. There were issues with Cl impurities, which could effect the results, and to be confident with the conclusions made in the paper the results have to be reproduced without any Cl involved. Additionally, a well defined surface with 0.5 ML should be used as a coverage calibration, which we was not able to do in Paper V. The influence of steps could be more systematically investigated with the use of curved copper single crystals, for which several facets of Cu(n11) and Cu(n10) could be investigated.

Experiments were planed for SXRD measurements on the oxidation of Cu(911)

and Cu(100) with CO_2. The idea was to try to recreate the structures reported on Cu(911) and Cu(100), but with CO_2. However, these experiments were not successful as it was not possible to have pure enough CO_2 gas at the beamline. However, if the same purity of CO_2 as for the AP-XPS studies could be achieved at the SXRD beamlines, SXRD experiments could prove valuable in the study of CO_2 interaction with Cu.

A promising approach to further the development of new and more efficient catalyst is to investigate so-called single-atom alloys, where the properties of catalytically active materials are altered by doping them into more inert materials, such that the active material is atomically dispersed in the surface layer [46]. It has been shown that the clean $Cu_3Au(100)$ surface spontaneously exposes a surface structure similar to a single-atom alloy, consisting of 50% Cu atoms and 50% Au atoms [47]. Additionally, it has been found that the reduction of CO_2 to CO on a Cu-Au alloy increases compared to pure Cu or Au, which is attributed to the improvement of CO_2 dissociation associated with Cu [48]. Hence, an investigation of $Cu_3Au(100)$ in a similar manner done with Cu(100) in this thesis could be a promising approach to gain valuable knowledge.

Bibliography

[1] G. Centi, S. Perathoner, S. Gross, and E. J. M. Hensen. *Science and technology roadmap on catalysis for Europe: A path to create substaniable future.* European Cluster on Catalysis. ERIC aisbl. 2016.

[2] G. Bozzano and F. Manenti. Efficient methanol synthesis: Perspectives, technologies and optimization strategies. *Prog. Energy Combust. Sci.* **56** (2016), 71-105.

[3] B. Lindstrom and L. J. Petterson. A brief history of catalysis. *CATTECH* **7** (2003), 130-138.

[4] A.J.B. Robertson. The Early History of Catalysis. *Platinum Metals Rev.* **19** (1975), 64-69.

[5] J. Wisniak. The History of Catalysis From the Beginning to Nobel Prizes. *Educ. quím.* **21** (2010), 60-69.

[6] G. Lamoine. *Ann. Chim. Phys.* **12** (1877), 145.

[7] I. Chorkendroff and J. W. Niemantsverdriet. *Concepts of Modern Catalysis and Kinetics*. WILEY-VCH. 2nd eddition.

[8] M. Bowker. *The Basis and Application of Heterogeneous Catalysis*. Oxford University Press.

[9] G. Centi and S. Perathoner. Opportunities and prospects in the chemical recycling of carbon dioxide to fuels. *Catal. Today* **148** (2009), 191-205.

[10] M. D. Porosoff, B. Yan, and J. G. Chen. Catalytic reduction of CO_2 by H_2 for synthesis of CO, methanol and hydrocarbons: challenges and oppotunities. *Energy Environ. Sci.* **9** (2016), 62-73.

[11] J. Ma, N. Sun, X. Zhang, N. Zhao, F. Xiao, W. Wei, and Y. Sun. A short review of catalysis for CO_2 coversion. *Catal. Today* **148** (2009), 221-231.

[12] W. Taifan, J.-F. Boily, and J. Baltrusaitis. Surface chemistry of carbon dioxide revisited. *Surf. Sci. Rep.* **71** (2016), 595-671.

[13] B. Eren, R. S. Weatherup, N. Liakakos, G. A. Somorjai, and M. Salmeron. Dissociative Carbon Dioxide Adsorption and Morphological Changes on Cu(100) and Cu(111) at Ambient Pressures. *J. Am. Chem. Soc.* **138** (2016), 8207-8211.

[14] W. Wang, S. Wang, X. Ma, and J. Gong. Recent advances in catalytic hydrogeneration of carbon dioxide. *Chem. Soc. Rev.* **40** (2011), 3703-3727.

[15] P. Hofmann. *Solid State Physics: An Introduction.* WILEY-VCH. 1st edition.

[16] G. Attard and C. Barnes. *Surfaces*. Oxford Science Publications.

[17] C.-L. Liu. Energetics of diffusion processes during nucleation and growth for the Cu/Cu(100) system. *Surf. Sci.* **316** (1994), 294-302

[18] H. Ibach. *Physics of Surfaces and Interfaces*. Springer.

[19] G.-C. Wang, L. Jiang, Y. Morikawa, J. Nakamura, Z.-S. Cai, Y.-M. Pan, and X.-Z. Zhao. Cluster and periodic DFT calculations of adsorption and activation of CO_2 on the Cu(*hkl*) surfaces. *Surf. Sci.* **570** (2004), 205-217.

[20] S. Funk, B. Hokkanen, J. Wang, U. Burghaus, G. Bozzolo, and J. E. Garcés. Adsorption dynamics of CO_2 on Cu(110): A molecular beam study. *Surf. Sci.* **600** (2006), 583-590.

[21] J. Nakamura, J. A. Rodriguez, and C. T. Campbell. Does CO_2 dissociativly adsorb on Cu surfaces?. *J. Phys.: Condens. Matter* **1** (1989), 149-160.

[22] P. B. Rasmussen, P. A. Taylor, and I. Chorkendorff. The interaction of carbon dioxide with Cu(100). *Surf. Sci.* **269/270** (1992), 352-359.

[23] K. Hermann. *Crystallography and Surface Structure: An Introduction for Surface Scientists and Nonoscientists*. WILEY-VCH. 2nd eddtion.

[24] A. Groß. *Theoretical Surface Scinece: A Microscopic Perspetive*. Springer. 2nd eddition.

[25] C. Gattinoni and A. Michaelides. Atomistic details of oxide surfaces and surface oxidation: the example of copper and its oxides. Surf. Sci. Rep. **70** (2015) 424–447.

[26] J. A. Eastman, P. H. Fouss, L. E. Rehn, P. M. Baldo, G.-W. Zhou, D. D. Fong, and L. J. Thompson. Early-stage suppression of Cu(001) oxidation. *Appl. Phys. Lett.* **87** (2005) 051914.

[27] J. C. Yang, M. Yeadon, B. Kolasa, and J. M. Gibson. Oxygen surface diffusion in three-dimensional Cu_2O growth on Cu(001) thin films. *Appl. Phys. Lett.* **70** (1997) 3522- 3524.

[28] J.C. Yang, M. Yeadon, B. Kolasa, and J.M. Gibson. The Homogeneous Nucleation Mechanism of Cu_2O on Cu(001). *Scr. Mater.* **38** (1998) 1237-1242.

[29] G. W. Zhou. TEM investigation of interfaces during cuprous island growth. *Acta Mater.* **57** (2009) 4432-4439.

[30] U. Burghaus. Surface chemistry of CO_2 - Adsorption of carbon dioxide on clean surfaces at ultrahigh vacuum. *Prog. Surf. Sci.* **89** (2014), 161-217.

[31] S. Vollmer, G. Witte, and C. Wöll. Determination of site specific adsorption energies of CO on copper. *Catal. Lett.* **77** (2001), 97-101.

[32] J. Als-Nielsen and D. McMorrow. *Elements od Modern X-ray Physics.* Wiley. Second edition.

[33] S. Hüfner. *Photoelectron Spectroscopy: Principles and Applications.* Springer. 3th eddition.

[34] The Nobel Prize in Physics 1921. Nobel Media AB 2019. https://www.nobelprize.org/prizes/physics/1921/summary/, accessed Sun. 6 Jan 2019.

[35] The Nobel Prize in Physics 1981. Nobel Media AB 2019. https://www.nobelprize.org/prizes/physics/1981/summary/, accessed Sun. 6 Jan 2019.

[36] A. Zangwill. *Physics at surfaces.* Cambridge, Cambridge Univ. Press, 1988.

[37] S. Siegbahn, C. Nordling, G. Johansson, J. Hedman, P. F. Heden, K. Hamrin, U. Gelius, T. Bergmark, L. O. Werme, R. Manne, and Y. Baer. ESCA Applied to Free Molecules, North-Holland Publishing Company, Amsterdam (1969).

[38] D. F. Ogletree, H. Bluhm, G. Lebedev, C. S. Fandley, Z. Hussain, and M. Salmeron. A Differentially pumped electrostatic lens system for photoemission studies in the millibar range. *Rev. Sci. Instrum.* **73** (2002), 3872.

[39] The Nobel Prize in Physics 1986. Nobel Media AB 2019. https://www.nobelprize.org/prizes/physics/1986/summary, accessed Fri. 4 Jan 2019.

[40] B. Voigtländer. *Scanning Probe Microscopy: Atomic Force Microscopy and Scanning Tunneling Microscopy*. Springer. 2015.

[41] H. Möning, M. Todorović, M. Z. Baykara, T. C. Schwendenmann, L. Rodrigo, E. I. Altman, R. Pérez, and U. D. Schwarz. Understanding Scanning Tunneling Microscopy Contrast Mechanisms on Metal Oxides: A Case Study. *ACS Nano* **7** (2013), 10233-10244.

[42] P. Hofmann. Surface Physics: A Introduction. Version 1.3.

[43] P. Hohenberg and W. Kohn. Inhomogeneous Electron Gas. *Phys. Rev.* **136** (1964), 864-871.

[44] W. Kohn and L. J. Sham. Self-Consistent Equations Including Exchange and Correlation Effects. *Phys. Rev.* **140** (1964), 1133-1138.

[45] K. Reuter and M. Scheffler. Composition, structure, and stability of $RuO_2(110)$ as a function of oxygen pressure. *Phys. Rev. B* **65** (2002), 035406-03540611.

[46] G. Giannakakis, M. Flytzani-Stephanopoulos and E. C. H. Sykes. Single-Atom Alloys as a Reductionist Approach to the Rational Design of Heterogeneous Catalysts, *Acc. Chem. Res.* **52** (2019), 237-247.

[47] L. G. Dias, A. A. Leitão, C. Achete, R. Blum, H. Niehus, R. Capaz. Chemical identification in the $Cu_3Au(100)$ surface using scanning tunneling microscopy and first-principles calculations. *Surf. Sci.* **610** (2007), 5540-5545.

[48] E. Andrews, Y. Fang, J. Flake. Electrochemical reduction of CO_2 at CuAu nanoparticles: size and alloy effects. *J. Appl. Electrochem.* **48** (2018), 435-441.